In-operation Field of view Retrieval (IFR) for satellite and ground-based DOAS-type instruments applying coincident high-resolution imager data

Holger Sihler[1,2], Peter Lübcke[2], Rüdiger Lang[3], Steffen Beirle[1], Martin de Graaf[4,5], Christoph Hörmann[1], Johannes Lampel[1], Marloes Penning de Vries[1], Julia Remmers[1], Ed Trollope[3,6], Yang Wang[1], and Thomas Wagner[1]

[1]Max Planck Institute for Chemistry (MPIC), Hahn-Meitner-Weg 1, 55128 Mainz, Germany
[2]Institute of Environmental Physics (IUP), University of Heidelberg, Im Neuenheimer Feld 229, 69120 Heidelberg, Germany
[3]European Organisation for the Exploitation of Meteorological Satellites (EUMETSAT), Eumetsat Allee 1, 64295 Darmstadt, Germany
[4]Royal Netherlands Meteorological Institute (KNMI), Utrechtseweg 297, 3731 GA De Bilt, The Netherlands
[5]Delft University of Technology (TU-Delft), Stevinweg 1, 2628 CN Delft, The Netherlands
[6]Telespazio VEGA Deutschland GmbH, Europaplatz 5, 64293 Darmstadt, Germany

Correspondence to: H. Sihler (holger.sihler@mpic.de)

Abstract.

Knowledge of the field of view (FOV) of a remote sensing instrument is particularly important when interpreting their data and merging them with other spatially referenced data. Especially for instruments in space, information on the actual FOV, which may change during operation, may be difficult to obtain. Also, the FOV of ground-based devices may change during
5   transportation to the field site, where appropriate equipment may be unavailable.

This paper presents an independent, simple and robust method to retrieve the FOV of an instrument during operation, i. e. the two-dimensional sensitivity distribution, sampled on a discrete grid. The method relies on correlated measurements featuring a significantly higher spatial resolution, e. g. by an imaging instrument accompanying a spectrometer. The method was applied to two satellite instruments, GOME-2 and OMI, and a ground-based differential optical absorption spectroscopy
10 (DOAS) instrument integrated in an SO_2-camera. For GOME-2, quadrangular FOVs could be retrieved, which almost perfectly match the provided FOV edges after applying a correction for spatial aliasing inherent to GOME-type instruments. More complex sensitivity distributions were found at certain scanner angles, which are probably caused by degradation of the moving parts within the instrument. For OMI, which does not feature any moving parts, retrieved sensitivity distributions were much smoother compared to GOME-2. A 2D super-Gaussian with six parameters was found to be an appropriate model to describe
15 the retrieved OMI FOV. The comparison with operationally provided FOV dimensions revealed small differences, which could be mostly explained by the limitations of our IFR implementation. For the ground-based DOAS instrument, the FOV retrieved using SO_2-camera data was slightly smaller than the flat-disc distribution, which is assumed by the state-of-the-art correlation technique. Differences between both methods may be attributed to spatial inhomogeneities.

In general, our results confirm the already deduced FOV distributions of OMI, GOME-2 and the ground-based DOAS. It
20 is certainly applicable for degradation monitoring and verification exercises. For satellite instruments, the gained information

is expected to increase the accuracy of combined products, where measurements of different instruments are integrated, e. g. mapping of high-resolution cloud information, incorporation of surface climatologies. For the SO_2-camera community, the method presents a new and efficient tool to monitor the DOAS FOV in the field.

1 Introduction

5 The instantaneous field of view (IFOV) of an optical instrument describes the solid angle from which radiation is perceived by a detector. If the instrument is moving, averaging the IFOV over the integration time of one measurement yields the field of view (FOV). The term FOV used here refers to the spatial sensitivity distribution of the acquisition method rather than the distinct transfer properties of a point source through an optical system, which are usually referenced as point spread function (PSF), spatial transfer function, modulation transfer function (MTF), or impulse response of a system. In practice, the FOV is

10 often assumed quadrangular or elliptic with a constant sensitivity inside and zero sensitivity outside. This study demonstrates that this is a strong simplification and that some spectroscopic instruments feature a more complex FOV.

For satellite measurements, the extent and shape of the FOV are of particular interest in order to register the measured quantity in space. Accurate data registration is an important prerequisite for further data processing and comparison with other geo-referenced data. In principle, a-priori information on the IFOV is available from measurements in a controlled environment or

15 raytracing simulations(e. g. te Plate et al., 2001; Xiong et al., 2005; Dobber et al., 2006; EUMETSAT, 2011b; Wolfe et al., 2013), e. g. OMI (te Plate et al., 2001; Dobber et al., 2006), MODIS (Xiong et al., 2005), GOME-2B (EUMETSAT, 2011b), and VIIRS (Wolfe et al., 2013). The FOV then follows from geometric considerations. The alignment of the optical components, however, may change when deploying a satellite instrument in orbit or a ground-based based instrument in the field. Hence, it is desirable to infer the actual FOV at any time.

20 One possibility to obtain the FOV from measurements by the instrument itself is to scan over well-known edges and structures. For example, several methods to infer the FOV of imaging satellite instruments during operation (i. e. in-orbit) take advantage of man-made structures. McGillem et al. (1983) retrieved the PSF of Landsat imagery using field edges, Ruiz and Lopez (2002) derived the PSF by applying deconvolution filters to images of a large dam, and Campagnolo and Montaño (2014) exploited the linearity of dikes in the Netherlands. Another approach demonstrated by Wang et al. (2014) derived the

25 MTF of MODIS from scans of the lunar disk. For ground-based MAX-DOAS (Platt and Stutz, 2008), the vertical FOV shape and position are sometimes inferred from horizon scans provided that the horizon is visible and features a sufficiently strong radiometric gradient.

Spectrometers divide the electromagnetic spectrum into a much higher number of spectral channels (e. g. GOME-2: 4096) compared to imagers (e. g. MODIS: 36). The bandwidth of spectrometers is much smaller, and, hence, spectroscopic mea-

30 surements need a significantly larger integration time than imagers in order to achieve a similar signal-to-noise ratio (SNR) due to photon-statistics. The spatial resolution of spectroscopic instruments on satellites is, therefore, usually too coarse to use man-made structures or the moon for FOV retrievals.

For spectroscopic satellite retrievals, the FOV edges are assumed sharp in most applications (e. g. Koelemeijer et al., 1998; Kroon et al., 2008). This may be reasonable for scanning instruments like GOME, SCIAMACHY and GOME-2, but imaging spectrometers, like OMI, have a more complex, approximately bell-shaped FOV (Kurosu and Celarier, 2010). To address these peculiarities, Kuhlmann et al. (2014) developed an interpolation scheme for OMI data based on parabolic spline surfaces,

5 and Siddans (2016) proposed an approach to map high-resolution cloud data on TROPOMI measurements applying spectrally resolved FOVs obtained during pre-launch instrument calibration (Leloux, 2016). Furthermore, de Graaf et al. (2016) ~~presented an approach to infer~~ _obtained the_ parameters of a 2D super-Gaussian ~~distribution to characterise the FOV of OMI from MODIS measurements~~ _FOV by searching for maximum correlation between OMI and MODIS measurements (differences to this study are discussed in Sect. 4.2)._

10 For passive ground-based DOAS instruments using scattered solar light, the FOV is often characterised only in vertical direction using artificial line light sources, which is a sufficient approach for common multi-axis DOAS applications when the measurement signal is almost constant in lateral direction. This simplification, however, may become inappropriate when the DOAS instrument is used in combination with an imaging instrument, such as an SO_2-camera (Mori and Burton, 2006; Bluth et al., 2007; Kern et al., 2010). Built-in DOAS instruments are increasingly used to calibrate SO_2-camera images, because

15 DOAS measures SO_2 column densities more accurately due to the the technique's robustness with respect to interferences with other absorbers in the light path. The calibration procedure requires SO_2 column density measurements from both instruments accurately matched in space and time, i. e. the correlation between both measurements must be very high. In order to maximise the correlation, accurate knowledge of the FOV of the spectrometer within the SO_2-camera image is necessary. In the past, the FOV was often found by assuming a certain shape for the FOV – mostly a disk of varying diameter – and calculating the

20 correlation between the optical density and the SO_2 column density depending on disk diameter (e. g. Kern et al., 2010; Lübcke et al., 2013). However, this method is computationally expensive and an irregular shape of the spectrometer FOV can distort the results.

In this paper, we propose a method ~~that retrieves~~ _to retrieve_ discretised FOVs of ~~low-resolution~~ _spatially_ low-resolving (LR) spectrometers from correlated ~~high resolution~~ high-resolution (HR) measurements~~, where the term resolution refers to~~

25 _spatial_ ~~resolution.~~ _._ The In-operation FOV Retrieval (IFR) _method_ relies on a sufficiently large set of m inhomogeneous HR measurements, which need to be spatially aligned to the corresponding LR measurements. Three exemplary LR/HR _instrument_ combinations are investigated to demonstrate the applicability to both satellite and ground-based instruments: (1) GOME-2/AVHRR~~: GOME-2 is a scanning spectrometer, both instruments are borne by the same satellite~~, (2) OMI/MODIS~~: OMI is an imaging spectrometer, there is a delay of 8 minutes between both satellite acquisitions~~, and (3) passive DOAS/~~: both~~

30 ~~ground-based instruments are usually integrated into one device. The retrieval is in principle independent from the type of correlated information. Hence, we apply radiometric input data to retrieve the FOVs of both satellite instruments (Sect. 3.1 and Sect. 3.2) and optical densities of in the case of the (Sect. 3.3).~~

2 ~~Method~~

~~This section first provides an overview on the investigated~~ SO$_2$-camera.

The manuscript is organized as follows: Details on the instruments and data sets of these LR/HR combinations are provided in Sect. 2.1. Section 2.2 describes ~~how the non-uniform satellite imager data was resampled to the discrete FOV grid. After that, Sect. 2.3 details~~ the spatial resampling of the HR measurements, and the formal approach of IFR ~~followed by the error~~

5 ~~estimation~~ is explained in Sect. ~~A. The last~~ 2.3. Furthermore, Sect. 2.4 proposes a 2-dimensional ~~parametrisation of the OMI FOV~~ FOV parametrisation. The resulting FOV are presented in Sect. 3, and discussed in Sect. 4, for the considered LR/HR pairs, followed by the conclusions. Retrieval errors for the GOME-2 results are estimated in Appendix A.

2 Methods

2.1 Input data

10 #### 2.1.1 GOME-2/AVHRR

The first LR instrument, whose FOVs are investigated, is the second generation Global Ozone Monitoring Experiment ~~(GOME-2 Callies et a~~ GOME-2 is one of several instruments on the MetOp satellite. Two of the three essentially identical MetOp satellites are in orbit: MetOp-A and MetOp-B, which were launched in 2006 and in 2012, respectively. This study is limited to the GOME-2 instrument on MetOp-A.

15 GOME-2 features four spectroscopic main channels (science channels) between 240 and 790 nm with a spectral resolution between 0.26 and 0.51 nm. Furthermore, GOME-2 includes two polarisation measurement devices (PMDs) whose measurements are clustered to 15 PMD channels each (Lang, 2010; Tilstra et al., 2011). The instrument features a maximum swath width of 1920 km scanned applying the whisk-broom approach as depicted in Fig. 1. In July 2013, however, the nominal swath width of GOME-2 on MetOp-A was changed to 960 km.The IFOV in across-track ~~direction is~~ and along-track direction are

20 4 km and 40 km, respectively (Munro et al., 2016). One scan of GOME-2 consists of a 4.5 s forward-scan and a 1.5 s backward-scan divided into 24 and 8 pixels, respectively. Hence, the nominal pixel sizes of the four main science channels (MSCs) was $80 \times 40\,\text{km}^2$ before July 2013. The PMD readouts are performed at an 8 times higher rate, resulting in 256 PMD-pixels per scan leading to a nominal $10 \times 40\,\text{km}^2$ pixel for a forward-scan PMD pixel. It is noted that GOME-2 features a variable speed of the scanner motor in order to compensate for Earth curvature and to maintain a regular pixel size in across-track direction.

25 Furthermore, until June 2013, the swath width of GOME-2 was reduced to 240 km (narrow-mode) every 29 days providing an improved nominal resolution of $10 \times 40\,\text{km}^2$ for the ~~MCSs~~MSCs.

EUMETSAT provides coordinates representing the corners of a rectangular FOV for each GOME-2 measurement, i. e. one GOME-2 *pixel*, which is calculated from the readout timing and the scanner position. The FOV is typically assumed constant inside and zero outside the provided edges, respectively. The actual FOV edges, however, need to be shifted relative to the

30 provided FOV geo-locations depending on wavelength since the detector pixels are not read out simultaneously. This shift caused by the mirror movement during readout leads to the spatial aliasing effect (EUMETSAT, 2015c; Munro et al., 2016), whose influence on the radiometric correlation between HR and LR measurements has already been discussed by Koelemeijer
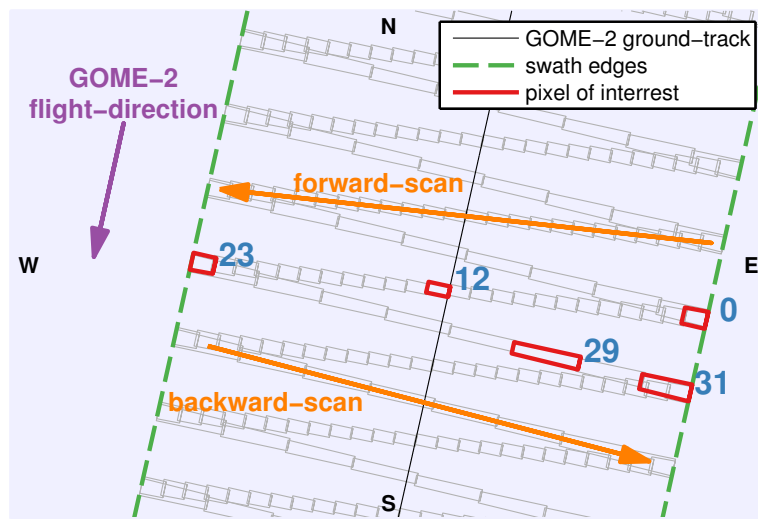
Figure 1. Schematic of GOME-2 whisk-broom scanning regime consisting of a 4.5 s forward-scan and a 1.5 s backward-scan. Note that the along-track displacement (along the flight direction) is enhanced by a factor of seven between the pixels for the sake of clarity – in reality, there are no gaps between consecutive forward-scans. The highlighted pixels are studied in more detail.

et al. (1998) for the first GOME instrument. The relative shift towards the subsequent FOV can be calculated from the detector pixel number for each detector (four MSC and two PMD detectors) separately. The detector pixel to wavelength mapping is provided in the data product and the calculation of the spatial aliasing is described in (EUMETSAT, 2015c; Munro et al., 2016). Effectively, the spatial aliasing for the MSCs is between zero and 26 % relative to the position of the succeeding FOV. The corresponding spatial offset of a nominal $80 \times 40\,\text{km}^2$ pixel is between 0 and 21 km in across-track direction.

The FOV of all nominal 32 MSC pixels were retrieved, but both narrow-mode FOV and PMD FOV were only retrieved in nadir direction. At nadir, neighbouring FOVs are very similar, and, therefore, the accuracy could be improved by combining neighbouring pixels of the same scan for narrow-mode and PMD FOVs. The four neighbouring pixels east and west of the nadir pixel were included in the FOV retrieval of the same nadir pixel for a nine-fold number of measurements m. This approach was particularly useful to reduce the time period required to retrieve the narrow-mode FOV because the narrow-mode is activated only every 29th day . Without averaging neighbouring pixels, more than one year of GOME-2 would have been required to gather $m=10^5$ measurements (see below).

In this study, the GOME-2 FOVs were retrieved from the combination with measurements by the AVHRR/3 (Advanced Very High Resolution Radiometer) instrument also installed on the MetOP-A satellite (EUMETSAT, 2011a) (Cracknell, 1997; NOAA, 2009; EU AVHRR features a nadir resolution of 1.1 km and acquires data in five spectral channels between the visible red and thermal infra-red (NOAA, 2014). The first two channels of AVHRR are used in this study because only these both overlap with the spectral range covered by GOME-2 as illustrated in Fig. 2. The spectral response of AVHRR channel 1 centred at 630 nm is
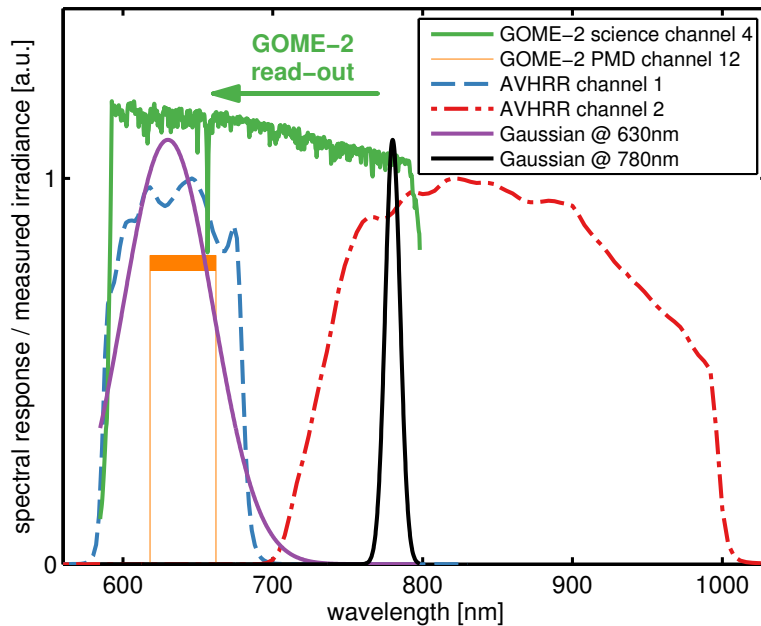
Figure 2. Solar irradiance spectrum measured by science channel 4 of GOME-2 on 1 April 2009, the spectral range covered by GOME-2 PMD channel 12, and the sensitivity response of AVHRR/MetOp channels 1 and 2 (Lang, 2010; NOAA, 2014). In addition, two Gaussians used to convolve GOME-2 spectra are shown.

almost entirely located within GOME-2 science channel 4 at its left edge. The spectral response of AVHRR channel 2, however, exceeds that of GOME-2 channel ~~2~~ 4 towards the infra-red.

Five different spectral convolution kernels were applied to MSC 4 data of GOME-2 in order to investigate the correlation between GOME-2 and AVHRR radiances and the trade-off between minimising spatial aliasing and maximising spectral overlap

5 between GOME-2 and AVHRR: ~~The~~ the spectral response of AVHRR channels 1 and 2 (NOAA, 2014), the spectral response of PMD channel 12 approximated by a box-profile between 618 and 662 nm (Lang, 2010), one Gaussian centred at 630 nm and 30 nm width, and one Gaussian at 780 nm and 5 nm width (depicted in Fig. 2). It is noted that the readout direction of MSC 4 is inverted, i. e. the read-out starts at 790 nm and proceeds towards shorter wavelengths (cf. green arrow in Fig. 2). Hence, radiances at the right edge of MSC 4 would be ideal in order to minimize spatial aliasing. But there, spectral correlation was

10 assumed inferior compared to the range overlapping with AVHRR channel 1. The most dominant feature between AVHRR channels 1 and 2 is the absorption by chlorophyll (red edge), and, therefore, data over land was optionally filtered from the FOV retrieval.

GOME-2 FOVs of nominal and narrow-mode MSC pixels were retrieved from $m = 10^5$ combined LR/HR measurements. For the PMD FOV, $m = 10^6$ measurements were collected. The time period required for data collection was different for all

15 three different pixel types due to the different measurement frequency and sample size m: (1) 1 to 21 April 2009 for nominal

MSC pixels, (2) 23 February, 24 March, and 22 April 2009 for the narrow-mode MSC pixel, and (3) 1 to 25 April 2009 for the nominal PMD pixel. AVHRR data was resampled on two different grids (Sect. 2.2): $4 \times 4\,km^2$ for nominal MSC pixels and $1.5 \times 2.5\,km$ for narrow-mode and PMD pixels.

2.1.2 OMI/MODIS

5   The second LR instrument investigated was OMI ~~(Ozone Monitoring Instrument Levelt et al., 2006)~~ (Ozone Monitoring Instrument, Levelt the NASA Aura satellite (Schoeberl et al., 2006). Compared to GOME-2, OMI features a wider swath of 2600 km covering the entire globe within one day without data gaps. OMI is an imaging spectrometer operated as a push-broom scanner. The UV-2/VIS channel of OMI divides the entire swath into 60 individual ground pixels of varying width. The nominal pixel size is ~~13~~24 $\times$ ~~24~~13 km^2 in nadir direction and increases towards the swath edges.

10   OMI data recorded after 25 June 2007 is potentially affected by the row anomaly (KNMI, 2015). This instrument anomaly affects level 1B radiances depending on viewing angle/pixel number and changes over time. In particular interest for this study, pixels 53 and 54 are affected since 25 June 2007 and pixels 37 through 42 are affected since 11 May 2008. The anomaly comprises a reduction or increase of the received radiance depending on latitude and with second-order effects. In this study, however, pixels possibly influenced by the row anomaly were included in the FOV retrievals nevertheless.

15   The OMPIXCOR data set obtained from NASA provides two sets of pixel edges for OMI: (a) *tiled* pixel edges, whose application results in a seamless swath image, and (b) overlapping *75FoV* pixel edges (Kurosu and Celarier, 2010). The across-track widths of both FOV models correspond to the full-width half-maximum (FWHM) of the actual FOV. For the 75FoV pixel edges, the edges are scaled in along-track direction so that 75 % of the theoretical along-track FOV fall within the pixel edges (Fig. 3). The theoretical along-track FOV is calculated by convolving a fourth-order super-Gaussian with a step-function

20   whose length corresponds to the movement of OMI during one pixel integration with respect to the surface (Kurosu and Celarier, 2010). At nadir, both edge-definitions produce similar results whereas FoV75 edges are approximately twice as large as tiled edges in along-track direction at the swath edge. It is noted by Dobber et al. (2006) that the polarisation scrambler device of OMI imposes non-uniform structures on the spatial response function, which lead to slightly polarisation dependent FOVs.

25   OMI radiances were compared to radiances recorded by the Moderate Resolution Imaging Spectroradiometer (MODIS) aboard the Aqua satellite (Salomonson et al., 1989). MODIS features a swath of 2330 km width, which is smaller than the OMI swath (Fig. 3). Therefore, it was not possible to evaluate the FOV of all OMI pixels. The outermost OMI pixels included in this study were pixel 3 and 56 at the western and eastern edge of MODIS, respectively. MODIS provides nadir resolutions of 0.25, 0.5, and 1 km depending on the channel. In this study, MODIS Band 3 (459–479 nm) was applied because it provides a

30   favourable resolution of 500 m in the sensitivity range of OMI as illustrated in Fig. 4.

Unlike the GOME-2/AVHRR instrument combination, OMI and MODIS are not observing simultaneously. However, Aqua and Aura are both part of the A-train constellation consisting of several spacecraft. Since May 2008, the delay between both observations is approximately 8 minutes (Schoeberl, 2002; NASA, 2014). This delay reduces the correlation between OMI and MODIS measurements because cloud scenes and illumination conditions change between overpasses. In order to increase the
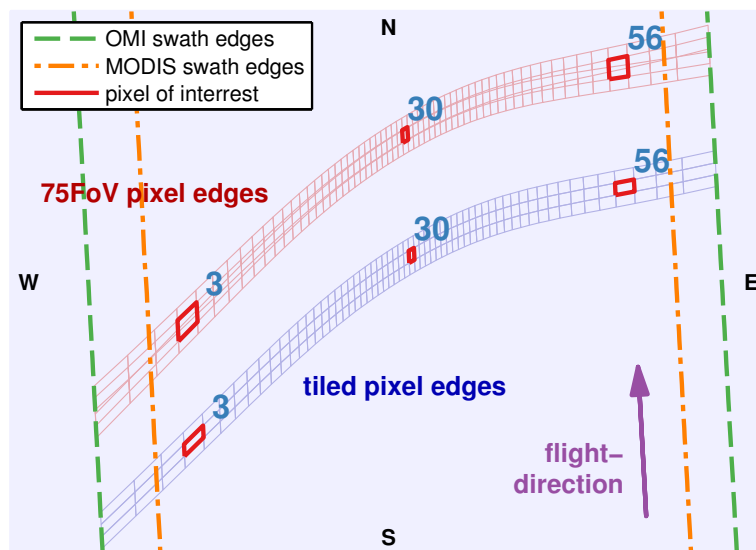
Figure 3. OMI and MODIS swath collocation since May 2008. Furthermore, two OMPIXCOR tiled pixel edges and 75FoV pixel edges are depicted. Note that the y-axis is enhanced by a factor of four for the sake clarity. Pixels highlighted in red are studied in more detail.

correlation, combined LR/HR observations with an increased probability of significant cloud movement were filtered by using wind-speed interpolated from the global meteorological circulation model maintained by the European Centre for Medium-Range Weather Forecasts (ECMWF). ~~Scene measurements~~ Measurements of scenes in which the interpolated maximum wind-speed between 1 and 3 km altitude exceeds ~~the~~ a certain wind-speed threshold t_w ~~=15m/s were filtered~~ were discarded in order to decrease the effect of cloud movement between overpasses. For the retrieval of OMI FOVs, 10^5 OMI (LR) and coincident MODIS (HR) measurements were collected between -60° and 60° latitude and between 1 and 9 October 2008 without taking the scene characteristics into account. Combined LR/HR measurements were subsequently filtered using the wind-speed filter. The application of the filter reduced the number of independent observations by $\approx 25\,\%$ to $m \approx 7.5 \times 10^4$. MODIS data was resampled on a $2 \times 2\,\mathrm{km}^2$ grid (Sect. 2.2).

2.1.3 MAX-DOAS/SO$_2$-camera

As third example, IFR was used to characterise the FOV of a ground-based ~~stray light~~ scattered radiation DOAS instrument, which was integrated in an SO$_2$-camera for calibration purposes (e. g. Kern et al., 2010; Lübcke et al., 2013). Figure 5 shows a schematic of the SO$_2$-camera-setup at volcanic plumes.

An SO$_2$-camera is an imaging instrument that uses two band-pass interference filters (with a FWHM of approximately 10 nm) to measure the optical density of SO$_2$. Images recorded with filter A (I_A) measure the optical density of SO$_2$, whereas images recorded with filter B (I_B) are used to correct for aerosol influences (Mori and Burton, 2006; Bluth et al., 2007).
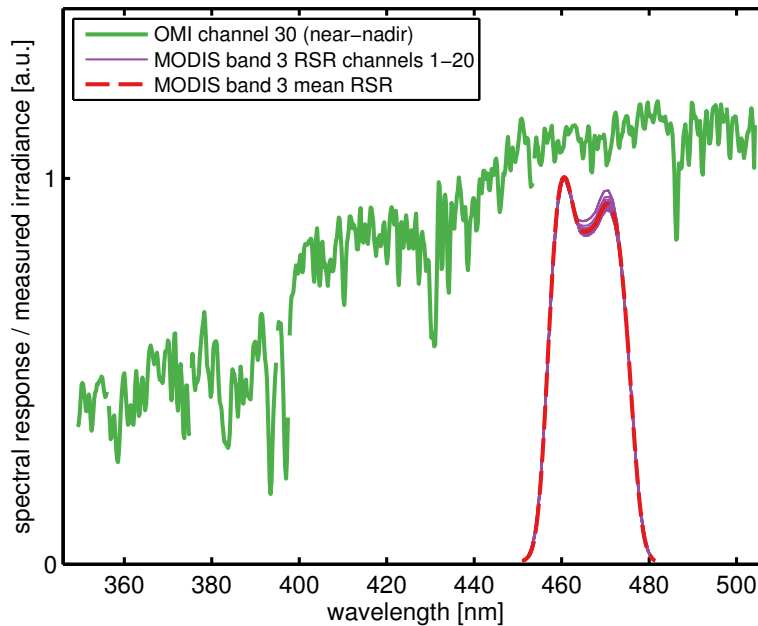
Figure 4. Solar irradiance spectrum measured by the VIS-channel of OMI on 1 April 2007 and the relative spectral response (RSR) of MODIS Aqua band 3 channels 1 through 20 (Barnes et al., 1998; Xiong et al., 2006, 2008).

Furthermore, two respective reference images $I_{A,0}$ and $I_{B,0}$ with negligible SO_2 absorption are required. Then, the apparent absorbance

$$\tau = -\ln\frac{I_A}{I_{A,0}} + \ln\frac{I_B}{I_{B,0}} \tag{1}$$

may be calculated (Kern et al., 2010). In case of negligible ash or aerosol concentrations in the plume, the second term in
5 Eq. 1) vanishes and the first term remains providing the optical density τ of SO_2 In order to calculate SO_2 emission rates, the instrument has to be calibrated, i. e., τ has to be converted to SO_2 column densities. This calibration is routinely done with help of a DOAS spectrometer (e. g. Kern et al., 2010; Lübcke et al., 2013; Kern et al., 2015a; Smekens et al., 2015), in particular for instruments that are permanently installed to monitor volcanoes (Kern et al., 2015b).

The SO_2-camera consists of a CCD detector, a fused-silica lens and two band-pass interference filters, its properties are
10 summarized in (Kern et al., 2015a) under the name HD-Custom. The complete FOV corresponding to 1024 detector pixels is 23.5° resulting in 0.023° per pixel. A OceanOptics USB2000 spectrometer with a narrow FOV (400 µm fibre diameter, 50 mm focal length, 0.46 ° opening angle) is co-located in the instrument's housing. The two filters were alternatively placed in the light path with a rotating wheel. Images were sequentially acquired with both filters. Filter A measured in a region around 315 nm, where sufficient solar radiation is available and SO_2 still has strong absorption features. Filter B measured around
15 330 nm, a region where the SO_2 absorption is negligible compared to the region of Filter A.
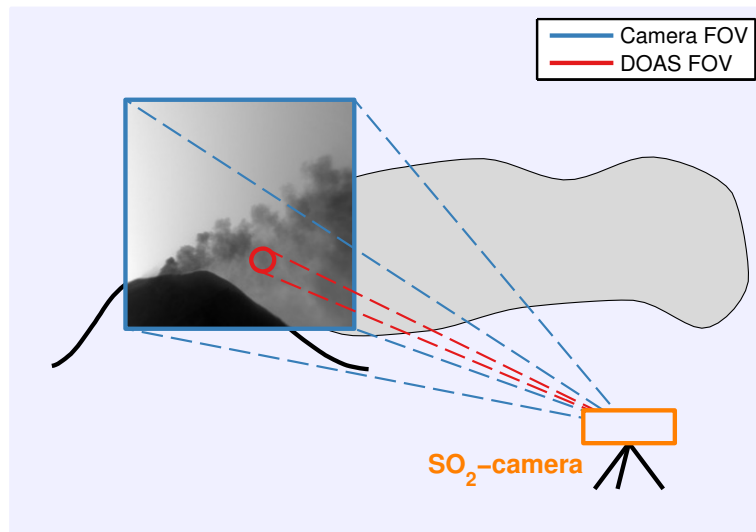
Figure 5. Schematic observation geometry of an SO_2-camera with included DOAS device for ground-based observations of volcanic plumes.

In this study, measurements are taken from the 12th IAVCEI Field Workshop on Volcanic Gases from Lastarria volcano ~~(Chile~~ in Chile (25°10'05" S, 68°30'25" W) on 21 November 2014. Between 13:39 and 15:30 UTC, a total of 2334 SO_2-camera images and 2424 LR spectra were recorded, respectively. For data evaluation, the images were reduced to an image size of 512×512 pixels resulting in $0.046°$ per pixel. Since the approximate location and size of the FOV were known, a further
5   subset of 128×128 pixels was used to determine the exact FOV.

In order to find the FOV of the spectrometer within the camera image, the SO_2 optical densities measured by the SO_2-camera (HR data) and the DOAS-spectrometer (LR data) were compared. Since the SO_2-camera and the spectrometer recorded data with a different time resolution, the intensities from the spectrometer were interpolated to match the acquisition times of the SO_2-camera images.

10 The IFR results are compared to the commonly used correlation method to find the FOV (Lübcke et al., 2013; Smekens et al., 2015). In the implementation of Lübcke et al. (2013), the FOV was found by varying the size and position of an a-priori circular FOV disk and calculating the correlation coefficient between the so-called apparent absorbance, i. e. the difference between the optical densities measured with Filter A and Filter B, and the SO_2 column density from the DOAS instrument.

2.2 Resampling of imager data

15 The IFR method described below (Sect. 2.3) requires correlated HR/LR measurements. Satellite HR measurements are usually not provided on a discrete, even-spaced euclidean grid. Therefore, HR data correlated to each LR measurement needs to be resampled to the same regular grid. HR data is required to cover the entire surface surrounding an a-priori FOV sampling region.

The region may be as large as the entire solid angle of the HR measurement provided it includes the actual FOV of the LR measurement. It is evident that a smaller time difference between HR and LR acquisition time increases their correlation and, hence, increases the SNR of the retrieval. For GOME-2/AVHRR and the SO_2-camera both measurements are nearly coincident providing a high correlation. OMI and MODIS, however, are operated from different satellites with different overpass times. Hence, special measures must be undertaken in order to exclude observations with large changes of the radiation field between the overpasses.

Satellite data is typically georeferenced in topocentric logitude/latitude coordinates. This data needs to be transformed into a x/y-grid relative to the pixel centre with N_x and N_y grid cells in x- and y-direction, respectively. For the sake of simplicity, HR measurements are assumed perfectly geolocated and point-like. In reality, however, HR measurements have a FOV size similar to their resolution. The HR resampling involves three steps:

1. transformation of latitude/longitude/radius ~~geolocations~~ coordinates to earth-centred ~~coordinates~~ $x/y/z$ coordinates applying the WGS84 ellipsoid (x-axis towards 90 °E, y-axis towards the north pole, z-axis towards zero meridian)

2. rotation of HR data into the $(0,0,z)$-centred x/y-plane using the corresponding LR ~~geolocations (see below),and average HR measurements within each grid cell.~~

~~The second step comprises 3 consecutive rotations as already pointed out by Siddans (2016) . The~~ coordinates similar to Siddans (2016) :

  (a) (x,y,z) LR pixel centre ~~, e.g. (~~point F in Fig. 6~~for GOME-2, is rotated~~), around y-axis to $(0,y',z')$

  (b) ~~(0,z) first. A third rotation along the z-axis aligns the LR pixel edges in the~~ $y',z')$ around x/y~~-plane,i.e. for GOME-2,the halfway points between point A and B as well as C~~ -axis to $(0,0,z'')$

  (c) rotation around z-axis so that the y-offset of both midpoints of the along-track pixel edges (M_1 and ~~D have the same y-offset (cf.~~ M_2 in Fig. 6~~), for OMI the *tiled*~~ pixel outlines are treated respectively. (b)) are equal

3. averaging of HR measurements within each grid cell.

Hence, one HR radiance image is obtained for each single LR measurement. The definitions of the rotations of step 2 apply for any common quadrangular pixel shape. Figure 6 shows an example of raw and resampled AVHRR data where the pixel centre and edges of GOME-2 were used as input for the projection. It needs to be noted that the choice of the HR grid is somewhat arbitrary – also irregular grid sizes are possible – but the resolution is constrained by original HR resolution and storage capacity. In this study, quadratic grids are mostly chosen for the sake of simplicity.

AVHRR data was resampled for the FOV retrieval of a variety of GOME-2 pixels. In principle, AVHRR delivers 1.1 km resolution at nadir, but the across-track resolution becomes poorer at the swath edges. Furthermore, the AVHRR revealed a very weak but systematic, almost alternating radiance offset depending on across-track scan position. This systematic bias perturbed the results because the same LR sub-pixel area was mapped always on the same AVHRR row. The errors became particularly apparent for retrievals at the swath edges. Therefore, a relatively coarse quadratic 4 km resolution was applied to
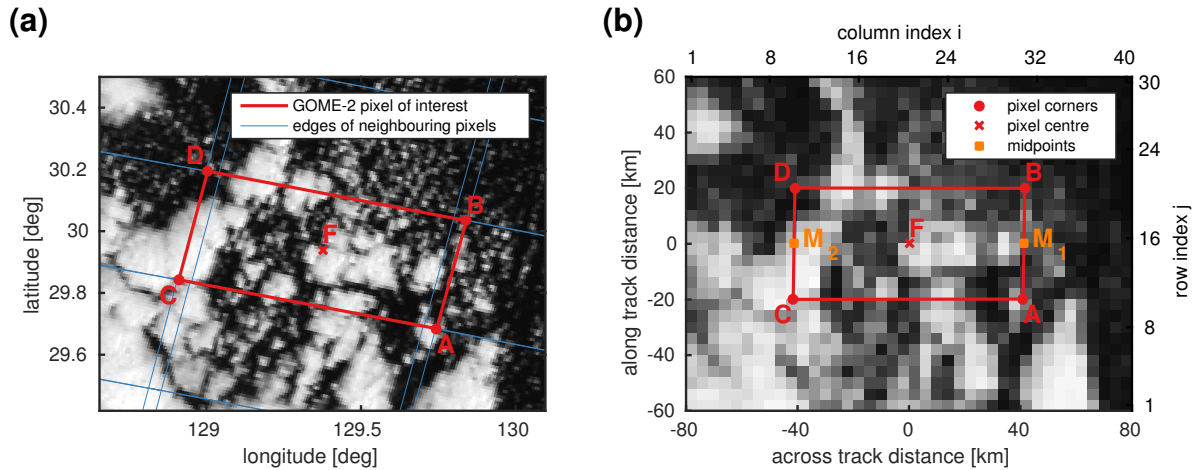
Figure 6. Geospatial alignment of AVHRR measurements and GOME-2 spatial sampling over an example area south of Japan on 2 April 2009: (a) AVHRR raw data in topocentric coordinates, Plate Carrée projection; (b) data projected and averaged on a $4 \times 4 \, km^2$ grid. The gray levels are extracted from AVHRR channel 1. GOME-2 pixel 12 in the swath centre is highlighted. ~~The letters denote the GOME-2 pixel corners and centre, respectively.~~

the retrieval of the FOV of the GOME-2 science channels. Alternatively, the across-track resolution was increased to 1.5 km for the FOV retrieval of narrow mode and PMD pixels, which were evaluated only in nadir direction where the distortion in the AVHRR data was found negligible.

MODIS data was resampled at a resolution of 2 km for the retrieval of all OMI FOV within the MODIS swath. In contrast,
5   there was no need to resample SO_2-camera images due to its constant alignment to the MAX-DOAS instrument by design. The resolution of the 1024×1024 full-format images was, however, reduced by a factor of 2 in both spatial dimensions in order to save computing resources.

2.3 In-operation FOV retrieval (IFR)

This section ~~details the derivation of~~ formulates the linear equation system (LES) used to invert a field of view pattern from a
10   set of m correlated HR/LR measurements.

~~To start off, a single~~ The i-th HR/LR measurement tuple ~~consisting of a HR image h_{ij} and the corresponding LR radiance l~~ consists of a LR radiance l_i, which is usually averaged over a selected wavelength range, ~~is regarded for the sake of simplicity. The size of~~ and the corresponding HR image h_{ij} with $j = 1 \ldots n$, where n is the number of pixels. It is required that the HR image ~~is $N_x \times N_y$ indexed by i and j in x and y direction, respectively~~ contains the entire LR FOV. ~~The assumption that l linearly depends on~~ If we assume an idealised linear response for both instruments, then l_i can be expressed as a linear combination of

h_{ij} ~~provides~~

$$l_i = \sum_{i=1}^{N_x} c_0 + \sum_{j=1}^{N_y} {}^{n} h_{ij} c_{ij\,j} \tag{2}$$

~~where c_{ij} are the unknown~~ with constant offset c_0, which adds a further degree of freedom compensating potential input biases due to instrumental deficiencies and imperfect radiance calibration, and discrete FOV coefficients c_j, which correspond to the fraction of radiation received from each particular solid angle or area within the ~~sampled range. Rearranging the double sum yields~~

$$l = c_0 + \sum_{k=1}^{n} h_k c_k$$

~~where n~~ HR image. Second order effects necessary to model effects like those caused by the row anomaly of OMI are neglected. Then, all ~~c_j with $j = N_x \cdot N_y$ is the number of FOV coefficients and c_0 is a constant, which is introduced in order to compensate potential input biases due to instrumental deficiencies and imperfect radiance calibration.~~

~~Equation (2) is linear, and, therefore,~~ $0\ldots n$ can be inferred from $m = n+1$ ~~linear independent HR/LR measurements (equations) are required to infer all c_k ($k=0,\ldots,n$). This leads to the LES~~ measurements by solving

$$
\begin{pmatrix} l_1 \\ \vdots \\ l_m \end{pmatrix}
=
\begin{pmatrix} 1 & h_{11} & \cdots & h_{1n} \\ \vdots & \vdots & & \vdots \\ 1 & h_{m1} & \cdots & h_{mn} \end{pmatrix}
\begin{pmatrix} c_0 \\ c_1 \\ \vdots \\ c_n \end{pmatrix}
\tag{3}
$$

or, in matrix notation,

$$\boldsymbol{l} = \mathbf{H}\boldsymbol{c} \tag{4}$$

where $\boldsymbol{l}$ contains the LR-radiances, $\mathbf{H}$ is ~~an~~ the $m \times (n+1)$ matrix containing the gridded HR-radiances, and $\boldsymbol{c}$ contains the $n+1$ discrete FOV coefficients. ~~Then, inverting~~

The inversion of Eq. (4) ~~yields the FOV coefficients $\boldsymbol{c}$. This straight forward inversion~~, however, is only successful if all input quantities were not significantly affected by measurement errors and rank $\mathbf{H} = n+1$. In reality, however, all input data contains errors – statistical ~~as well as systematic~~, systematic, and numeric – and different approaches exist to increase the stability of the solution. In this paper, two particular approaches are applied:

1. If the number of linearly independent measurements is $m > {\color{red}\sout{(n+1)}}\, n+1$, Eq. (4) yields a least-squares solution of

$$\min \|\boldsymbol{l} - \mathbf{H}\boldsymbol{c}\|_2 \tag{5}$$

using standard numerical approaches. For example, the software used for this study applies QR-factorization plus column pivoting to solve this numerical problem. The solution gained allows an error estimation described in Sect. A.

2. Sometimes~~it is not~~, it may not be possible to acquire a sufficiently large set of measurements, and thus the previous approach is not applicable. Then, however, it is still possible to calculate a solution for c under an additional regularisation constraint ~~in the underdetermined $m<n$ case~~. In this work, the iterative LSMR-method (Fong and Saunders, 2011) is applied to find a solution of the regularised least-square problem using a regularisation parameter λ. It is a follow up on the LSQR-method (Paige and Saunders, 1982). For this application, the parameter λ effectively balances signal-to-noise ratio and spatial bandwidth of the solution. The LSMR-solution converges towards the least-squares solution for small λ and sufficiently large m. The optimal choice of λ depends on the application, data quality, and quantity m.

The retrieved discrete FOV coefficients ~~c_{ij}~~ c_j were finally normalised to unit area of the x/y-grid. The resulting FOV fractions

$$c^{*}_{\underline{j}} = \frac{c_{ij}}{\Delta x \Delta y \sum_{i,j} c_{ij}} \frac{c_j}{\Delta x \Delta y \sum_j c_j} \tag{6}$$

correspond to the sensitivity contribution from grid cell ~~(i,j)~~ per km^2 or per pixel for satellite and SO$_2$-camera application, respectively.

2.4 Parametrised FOV

For OMI, the discretised FOV results were compared to a parametrised super-Gaussian FOV. Kurosu and Celarier (2010) describe the along-track FOV as the convolution of a flat-topped fourth order Gaussian IFOV with a box-car, which is adapted by Kuhlmann et al. (2014). The width of the box-car is 13 km corresponding to the travelled distance of the line-of-sight within one exposure of 2 s. In this study, for the sake of simplicity, the FOV was approximated using a generalised Gaussian model with variable exponent – sometimes referred to as a super-Gaussian model – instead of applying the convolution explicitly. This approximation yields a slightly different FOV shape in along-track direction. This drawback is outweighed by the advantage of having a single FOV model applicable to all OMI pixels instead of an explicit FOV model depending on viewing angle.

A generalised Gaussian function models the FOV in one dimension

$$F_{1D} : z_a(x) = \gamma \exp\left[-\left|\frac{x - a_3}{a_2}\right|^{a_1}\right] \tag{7}$$

with shape parameter a_1, width a_2, x-offset a_3, and amplitude γ. It is noted that F_{1D} is the Gaussian bell curve for $a_1 = 2$. Equation (7) is enhanced by another dimension and ~~two~~ three additional parameters yielding the final ~~two dimensional~~ two-dimensional FOV expression

$$
\begin{aligned}
F_{2D} : z(x,y) &= \gamma \, z_a(x) \, z_b(y) \\
&= \gamma \exp\left[-\left|\frac{x - a_3}{a_2}\right|^{a_1} - \left|\frac{y - b_3}{b_2}\right|^{b_1}\right]
\end{aligned} \tag{8}
$$

where parameter-sets a_i and b_i describe the FOV shape and position in x- and y-direction, respectively. Equation (8) yields ~~eight~~ seven parameters, which are derived from ~~2D IFR results c_k (k~~ IFR results c_j ($j = 1 \ldots n$, c_0 is discarded) using standard least-squares fitting methods.

It is noted that there are several possibilities to formulate a 2D superposition of 2 super-Gaussians. Equation (8) models a rectangular FOV, but it is also possible to simultaneously model skewness and tilt using linear coordinate transformations. Also elliptical FOVs can be realised.

The retrieved widths a_2 and b_2 correspond to the e-folding lengths of Eq. (7). These parameters are not very intuitive and therefore difficult to compare to the dimensions provided by the OMPIXCOR data (Kurosu and Celarier, 2010). The across-track pixel widths of OMPIXCOR are defined as the FWHM of the FOV. The across-track FWHM w_x can be computed using Eq. 7 via

$$w_x = 2a_2 \left(\ln 2\right)^{1/a_1} \tag{9}$$

where a_1 and a_2 are part of the fit output. Likewise, the along-track pixel dimension depends on the shape b_1 and width b_2, respectively. The 75 %-width w_y in y-direction fulfilling

$$\int_{-w_y/2}^{w_y/2} \exp\left[-\left|\frac{y}{b_2}\right|^{b_1}\right] \mathrm{d}y = \frac{3}{4} \int_{-\infty}^{\infty} z_b(y)\mathrm{d}y \tag{10}$$

corresponds to the definition of the OMPIXCOR 75FoV along-track width. w_y contains three quarters of the received ~~energy~~ radiance in along-track direction. Equation 10 was solved numerically.

3 Results

3.1 GOME-2

3.1.1 Main science channel pixels

This section presents FOV results for GOME-2 pixels 12 (nadir), 0 and 31 (forward-scan and backward-scan at eastern swath edge), and 23 (western swath edge) as depicted in Fig. 1. The results for all 32 MSC pixels are compiled in the Supplement.

As a first example, the FOV of GOME-2 MSC pixel 12 was characterised for two different convolution kernels. The results are depicted in Fig. 7. A clear rectangular FOV with expected dimension results from evaluating AVHRR channel 1 images and GOME-2 radiances applying a Gaussian convolution kernel centred at 630 nm (Fig. 7a). The spatial sensitivity inside the FOV is almost constant. The FOV edges, however, have an offset > 15 km, which is reasonably accounted for by the applied spatial aliasing correction. GOME-2 channel 4 data at larger wavelengths is less affected by spatial aliasing due to the shorter readout delay. Switching to 780 nm reduced the offset between the provided and the interpolated edges (Fig. 7b). Noise, however, increases significantly due to a larger spectral offset between LR and HR data compared to Fig. 7a, even though filtering input data over land could reduce the influence of the spectral offset in Fig. 7b to some extent. The influence of the LR spectral convolution ~~kernels~~ kernel and the number of measurements m is further investigated in ~~Sect. A1 in the Appendix~~ Appendix A. For the sake of smaller errors, further results for GOME-2 are obtained applying the 630 nm Gaussian convolution kernel for GOME-2 data and AVHRR channel 1.
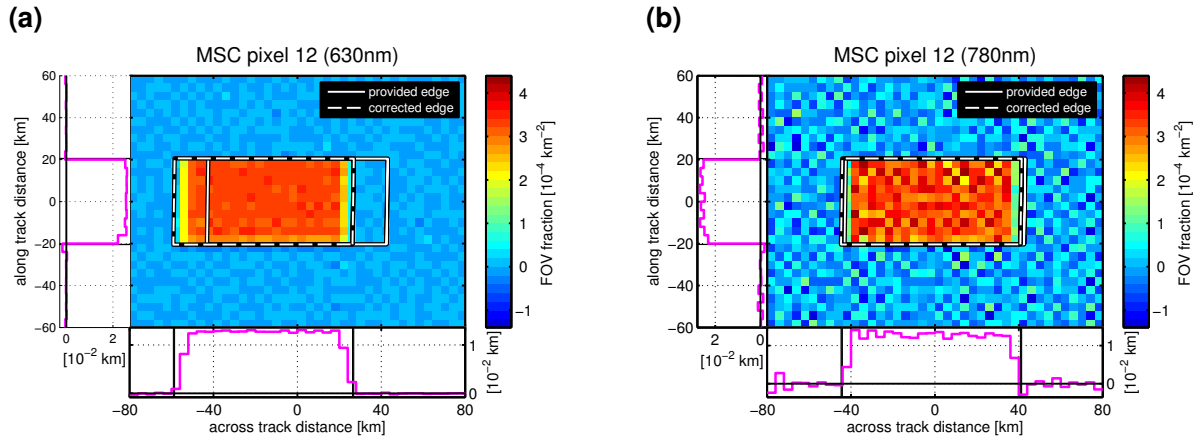
Figure 7. IFR results of GOME-2 MSC pixel 12 (nadir forward scan) at regular swath width inferred for two different LR convolution kernels: (a) Gaussian at 630 nm and (b) Gaussian at 780 nm. The input data for (b) only include measurements over ocean. The solid line denotes the pixel edges provided with the GOME-2 product whereas the dashed line denotes the interpolated pixel edges taking spatial aliasing into account. AVHRR channel 1 is applied as HR input for both images. The magenta lines in the panels below and left of the 2D FOV result denote across- and along-track integrals of the 2D results, respectively.

The FOV of the first forward-scan pixel is shown in Fig. 8(a). The retrieved FOV shape agrees with the provided pixel edges if spatial aliasing was corrected for. Otherwise, a spatial offset of ≈ 15 km was observed. The background noise in Fig. 8(a) is significantly larger than in Fig. 7(a) even though the number of HR/LR measurements m and the number of FOV nodes k were identical. This is due to a decreased HR/LR correlation, whose potential causes are discussed in Sect. 4.1.

5   The last forward-scan pixel in Fig. 8(b) reveals another interesting behaviour: The scan-mirror turns within the integration time-period of this pixel resulting in a comparatively inhomogeneous sensitivity within the FOV. Furthermore, due to the turning mirror, the spatial aliasing correction only needed to be applied to the eastern pixel edge resulting in a slightly smaller pixel. The retrieved FOV of the last backward-scan pixel 31 is shown in Fig. 9. It reveals an inhomogeneous sensitivity within the FOV again due to a turning scan mirror during integration. The spatial aliasing correction was only applied to the western
10   pixel edge.

3.1.2   Retrieval error over entire swath

After the investigation of the FOV of selected GOME-2 pixels, the scan-angle dependence of the reduced residual χ^2 (see Eq. A1) of each retrieved FOV is examined. Figure 10 summarises the χ^2 values for all 32 individual MSC pixels in the swath (cf. Fig.1). The plot shows that χ^2 is slightly increased for pixels at the swath edges, where the scanning direction changes
15   during integration, i.e. pixels 23 and 31 detailed in Figs. 8(b) and 9, respectively. More strikingly, Fig. 10 shows that IFR
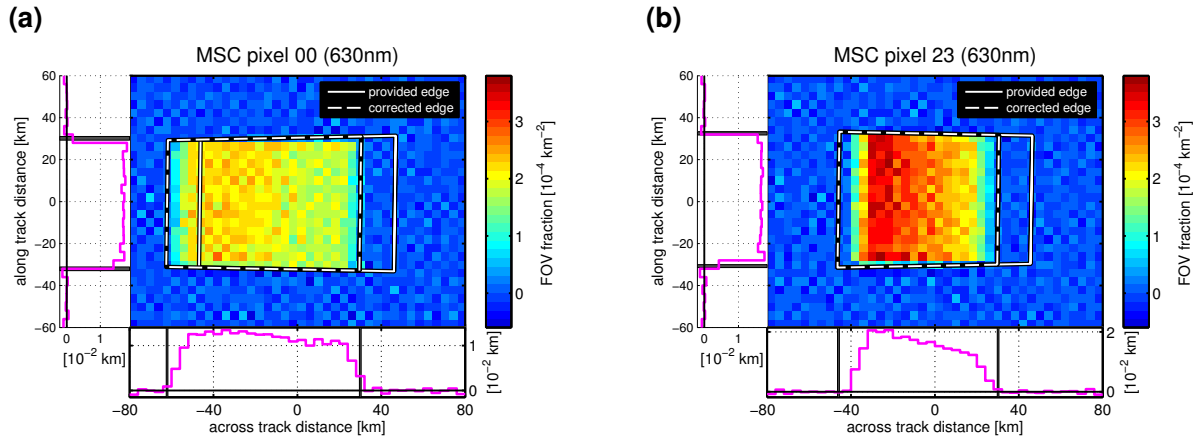
Figure 8. Same as Fig. 7(a) but for GOME-2 MSC swath edge pixels: (a) pixel 0 (first forward scan), and (b) pixel 23 (last forward scan). Note that the spatial aliasing correction in (b) is only applied for the eastern across-track edge as the mirror turns during integration.
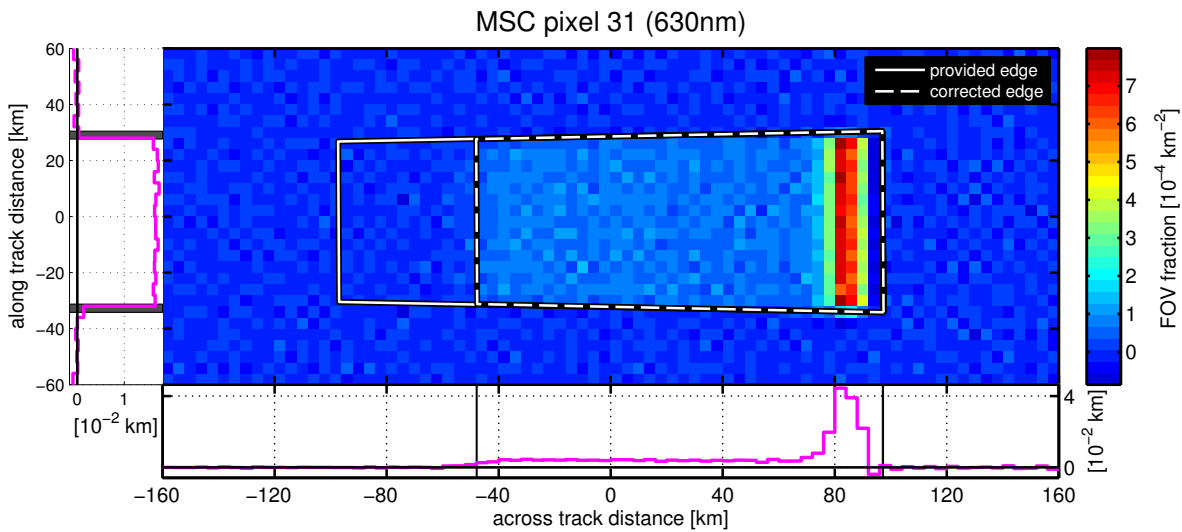
Figure 9. Same as Fig. 7(a) but for GOME-2 MSC pixel 31 (last backward scan). Note that the spatial aliasing correction is only applied for the western across-track edge as the mirror turns during integration.

results for pixels 5, 6, and 29 are of much lower quality compared to the other pixels. The respective χ^2-peaks in forward and backward direction are consistently located between -30 and -25 $^\circ$.
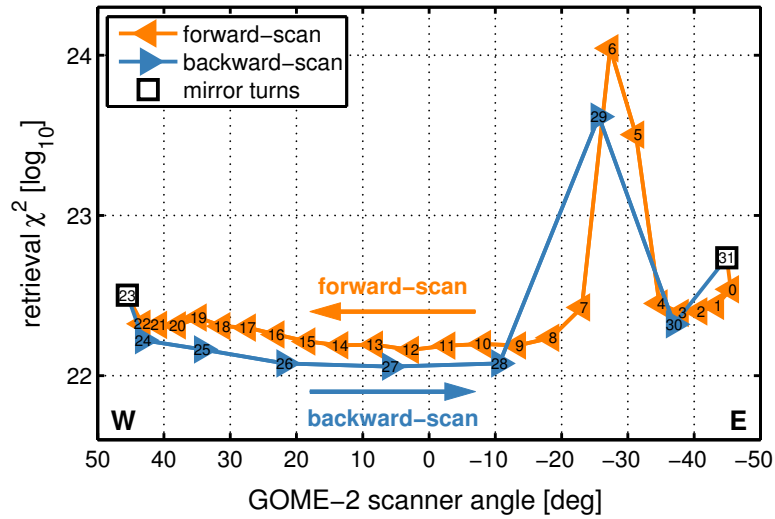
Figure 10. Retrieved χ^2 depending on GOME-2 scanner angle and pixel number (cf. Fig. 1) for the entire swath. The FOV residual increases between -30 and -25° potentially indicating telescope pointing instabilities in this range. The respective FOV result images are compiled in the Supplement.
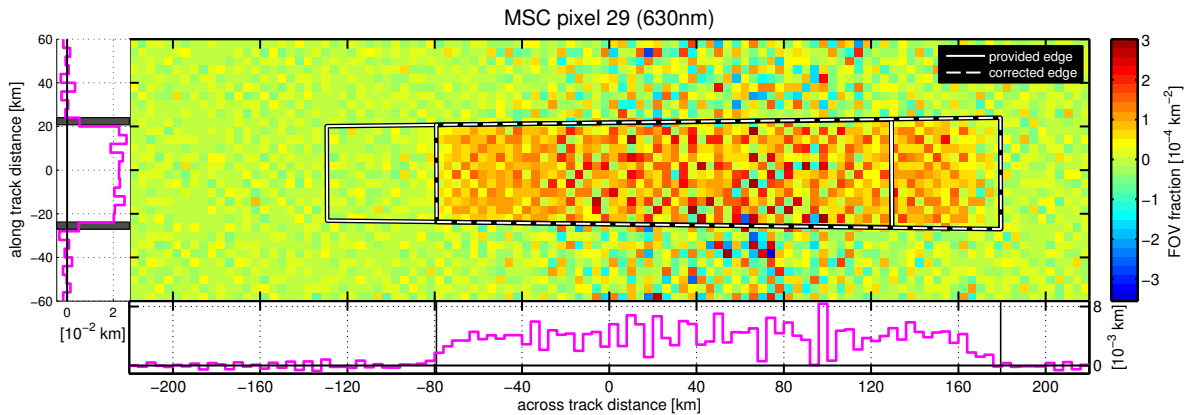
Figure 11. Same as Fig. 7(a) but for GOME-2 MSC pixel 29 revealing the strongest FOV distortions in the backward scan.

In order to further investigate increased FOV noise levels around -30°, Fig. 11 shows IFR result for the backward-scan pixel 29. The retrieved FOV is significantly distorted in an along track band between x = -40 and 120 km. This finding may be attributed to instrumental degradation, which is further discussed in Sect. 4.1.
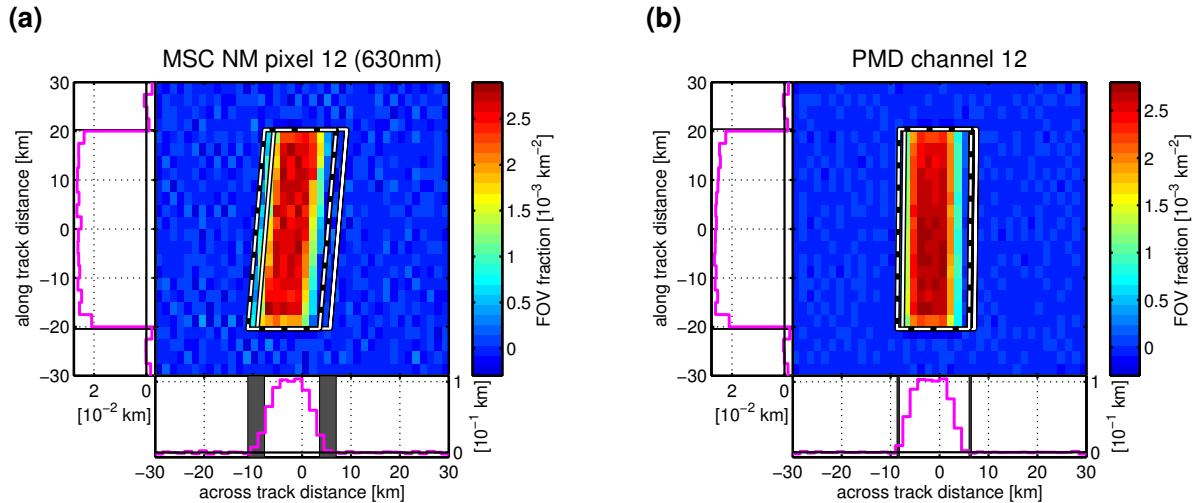
Figure 12. Same as Fig. 7(a) but (a) for an average MSC narrow-mode (NM) pixel at nadir (forward scan) and (b) for an average PMD-PP channel 12 pixel at nadir (forward scan). Note the different spatial resolution of $1.5 \times 2.5 \, \text{km}^2$.

3.1.3 Nadir narrow-mode MSC and PMD pixels

Both MSC narrow-mode and PMD FOVs have a nominal size of $10 \times 40 \, \text{km}^2$ in nadir direction. The observation modes, however, feature different optical paths, different detectors, and different scan mirror speeds. Also the FOV quadrangulars have different shapes – the narrow-mode pixel is more skewed than the PMD pixel – because the integration periods, during which

5 the spacecraft moves, are different for both pixel types by a factor of eight. For the retrieval of the MSC narrow-mode and PMD FOVs, HR data was resampled to a finer grid of $1.5 \times 2.5 \, \text{km}^2$ resolution to account for the eight times higher across-track resolution. It is noted that the PMD channel 12 was applied here as it features the best spectral overlap of all GOME-2 PMD channels with AVHRR channel 1 (cf. Fig. 2).

Figure 12a shows the average nadir FOV of the GOME-2 MSC in narrow-mode configuration. At this resolution, the FOV

10 quadrangular is clearly skewed. The PMD FOV in Fig. 12b is much less skewed due to a eight time shorter integration time and, hence, less influence of the satellite motion on the FOV shape.

Furthermore, the distribution of the sensitivity within the FOV was studied using across-track and along-track integrals of the FOV fractions as shown by the magenta lines in Figs. 12a and b. The narrow-mode MSC FOV is characterised by an almost constant box-car in along-track direction whereas the PMD FOV fraction drops by $\approx 5 \, \%$ for $> 10 \, \text{km}$. In across-track direction,

15 both narrow-mode and PMD FOVs reveal smoother edges than in along-track direction, especially at the eastern pixel edge of the PMD pixel. Furthermore, the PMD pixel appears to be significantly narrower than the provided pixel edges.

3.2 OMI

The design of the OMI satellite instrument is fundamentally different from GOME-2 as described in Sect. 2.1.2. Furthermore, the HR measurements by MODIS are taken 8 minutes after the OMI measurements deteriorating the correlation between both measurements. Therefore, the initial set of 10^5 combined measurements was filtered using a wind-speed threshold $t_w = 15$ m/s which proved to increase SNR of the FOV retrieval significantly. ~~The application of a more strict threshold, e.g. 10m/s, however, led to an SNR reduction due to the reduced statistics (cf. Fig. A2)~~ The choice of t_w was determined in preceding tests and presents a trade-off between discarding too many measurements, which would decrease SNR, and not filtering enough measurement necessary to reduce the smearing effect of scene changes due to cloud movement. The results can be considered robust as they only weakly depend on t_w.

Figure 13(a) shows the FOV results using the numerically exact LES solver. The SNR is much poorer compared to the result obtained from a similar sample size of GOME-2/AVHRR data (cf. Fig. 7). Therefore, the iterative LSMR method was applied as a fallback method because it computes approximate results while damping high spatial frequencies, and, hence, yields reduced retrieval noise. LSMR requires an additional parameter λ, which was empirically determined (cf. Sect. 3.2.2). Figures 13(b) through (d) show the retrieved FOV of pixel 30 in nadir direction depending on λ. The noise decreased with increasing λ. The result for $\lambda = 1 \times 10^{-3}$ (Fig. 13(d)) is comparatively smooth and the FOV distribution is almost 2D-Gaussian. The dependence on λ is investigated in more detail in Sect. 3.2.2.

3.2.1 Parametrised FOV

To compare OMI FOV shapes quantitatively, the retrieved FOV fractions were used as input to fit the FOV parametrisation of Eq. (8). An example fit output corresponding to Fig. 13(c) (OMI pixel 30, $\lambda = 3 \times 10^{-4}$) is compiled in Fig. 14. The residual in Fig. 14(b) indicates that the fit succeeded in finding a reasonable solution without significant contributions not captured by the FOV parametrisation.

Figures 14(c) and (d) show the integrated FOV cross-sections in across- and along-track direction, respectively. The shape of the retrieved FOV is well reproduced by the 2D fit (red line). However, there is a difference of shape, amplitude, and position between the theoretical and retrieved along-track ~~FOV and the retrieved shape~~ FOV in Fig. 14(d) due to the simplifications of the parametrised FOV model.

3.2.2 Dependence on λ

To test whether the fit results presented above are representative, the λ-dependence of the fitted FOV shape and width were investigated (Fig. 15). It is noted that the widths in across- and along-track direction w_x and w_y, respectively, were defined differently (Sect. 2.4). In across-track direction, the FWHM width w_x as defined by Eq. (9) is shown. In along-track direction, however, the 75 % width w_y was defined in analogy to the OMPIXCOR 75FoV pixel edge for better comparability. Equation (10) was used to calculate w_y from the fit-results.
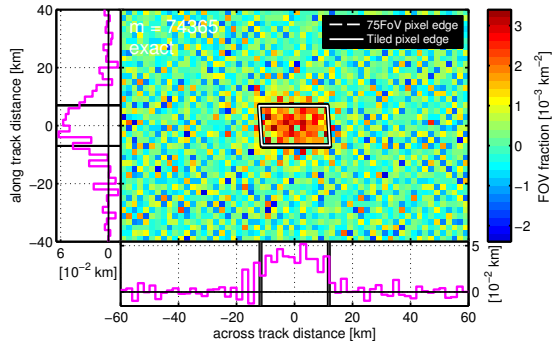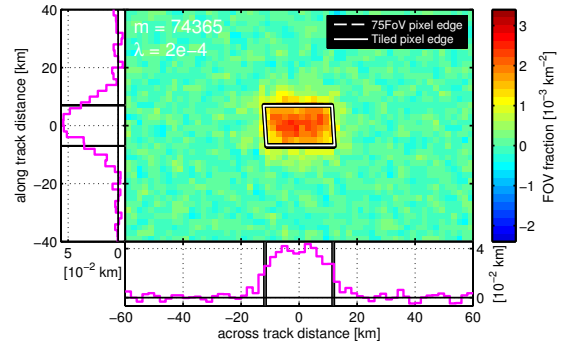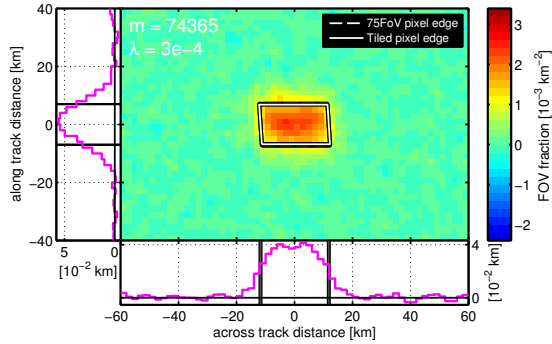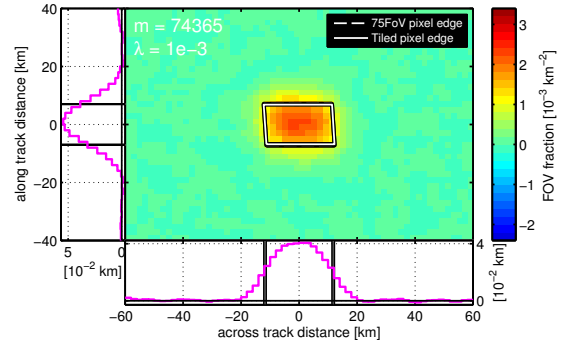
Figure 13. IFR results of OMI VIS channel pixel 30 (nadir) using different settings for the numerical inversion: (a) numerically exact solution, and (b) through (d) approximate LSMR solutions applying regularisation parameters $\lambda = 2 \times 10^{-4}$, 3×10^{-4}, and 1×10^{-3}, respectively ($t_w = 15$ m/s). It is noted that, for this observation geometry, the two OMI pixel coordinate products 75FoV (dashed line) and tiled (solid line) are almost identical.

In x-direction, the shape parameter a_1 features a plateau around 3.5 for $\lambda \leq 3 \times 10^{-4}$ before decreasing with increasing λ. The across-track width w_x is almost constantly 24 km for $\lambda \leq 1 \times 10^{-3}$ before increasing significantly towards larger λ.

In y-direction, the shape b_1 is again almost constant for $\lambda \leq 3 \times 10^{-4}$ at 2.1. Above $\lambda = 3 \times 10^{-4}$, b_1 increases slightly peaking at 2.3 at $\lambda = 3 \times 10^{-3}$. The along-track width w_y shows a dependence on λ similar to w_x, remaining almost constant for 5 $\lambda \leq 1 \times 10^{-3}$ and then increasing rapidly.

Smaller λ result in decreased SNR, larger λ reduce the resolution with smaller shape and larger width parameters. Hence, $\lambda = 3 \times 10^{-4}$ is assumed as a reasonable trade-off between noise and spatial resolution (cf. Figs. 13). It is noted that the observed behaviour of fitted shape and width was almost independent of t_w. For $t_w < 15$ m/s, shape parameters become slightly larger and widths are slightly (less than 1 km) smaller but the noise increases due to reduced statistics. Therefore, parameters $\lambda = 3 \times 10^{-4}$ 10   and $t_w = 15$ m/s were chosen for the results of the complete OMI swath (pixel 3–56), which are compiled in the Supplement.

(a) fitted 2D Super–Gaussian
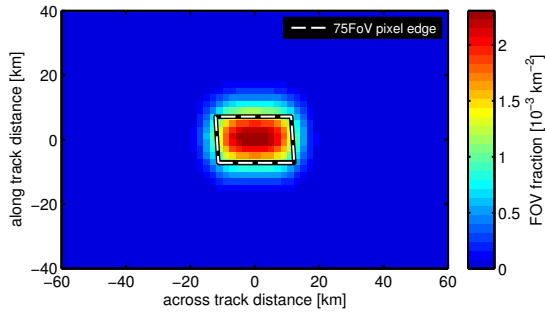
(b) fit residual
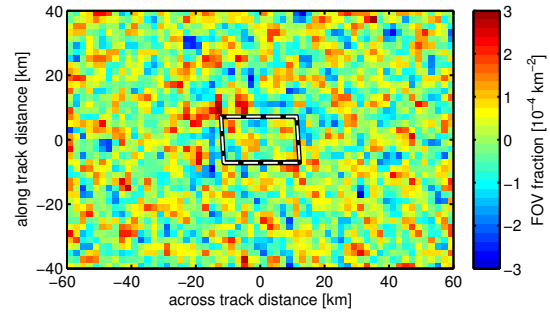
(c) across–track FOV
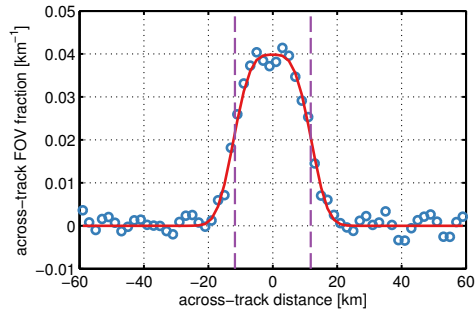
(d) along–track FOV
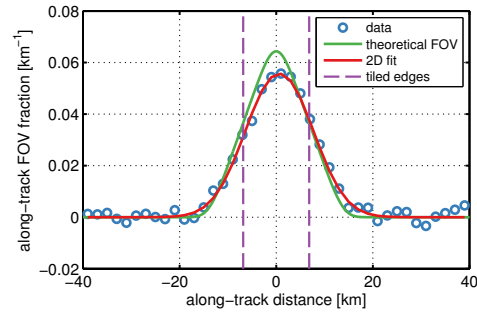
Figure 14. Fit of the nadir FOV results of OMI in Fig. 13: (a) fit result of the 2D FOV model in Eq. (8), (b) fit residual, (c) retrieved across-track FOV cross-section with 2D fit result compared to tiled pixel edges, and (d) retrieved along-track FOV cross-section with 2D fit result compared to theoretical FOV shape and tiled pixel edges ($\lambda = 3 \times 10^{-4}$, $t_\mathrm{w} = 15$ m/s). Note that (c) and (d) compare integrated results (blue dots correspond to the magenta lines in Fig. 13(c)), fit results, and theoretical FOV shape in across- and along-track direction, respectively.

3.2.3 Viewing angle dependence

In the following, the results for both extreme east and west viewing directions within the MODIS swath are presented. Figures 16(a) and (b) display the FOV of OMI pixels 3 (west) and 56 (east), respectively. Compared to pixel 3, the sensitivity of pixel 56 seems to be more heterogeneous and the background noise is larger. Both results reveal background structures,

5 which are periodic in along-track direction and probably caused by the multiple use of overlapping HR data corresponding to neighbouring LR pixels. The FOV maximum ~~approximates~~ in Fig. 16(b) is approximately at $x = -30$ km indicating an asymmetry in across-track direction. ~~Furthermore, Fig.~~Figures 16(a) and (b) ~~reveal another artefact:~~ furthermore show an increase of the integrated across-track FOVs (magenta line in the bottom panels) ~~increase~~ towards the borders ($x = \pm 120$ km). ~~An effect found more frequently~~ This behaviour becomes increasingly visible towards the swath edges (cf. Supplement) ~~. This behaviour~~

10 and is discussed in Sect. 4.2.
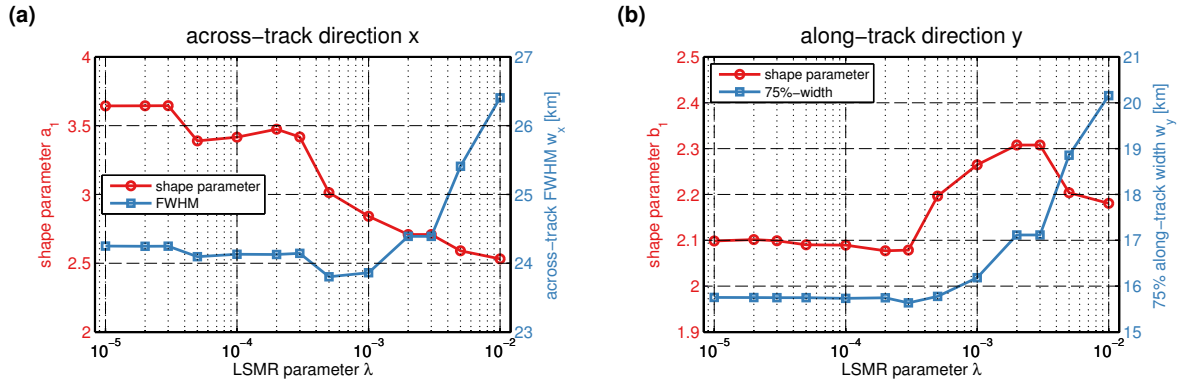
Figure 15. Fitted FOV shape and width for OMI pixel 30 (Fig. 13) depending on LSMR regularisation parameter λ in (a) across- and (b) along-track direction, respectively ($t_w = 15$ m/s).
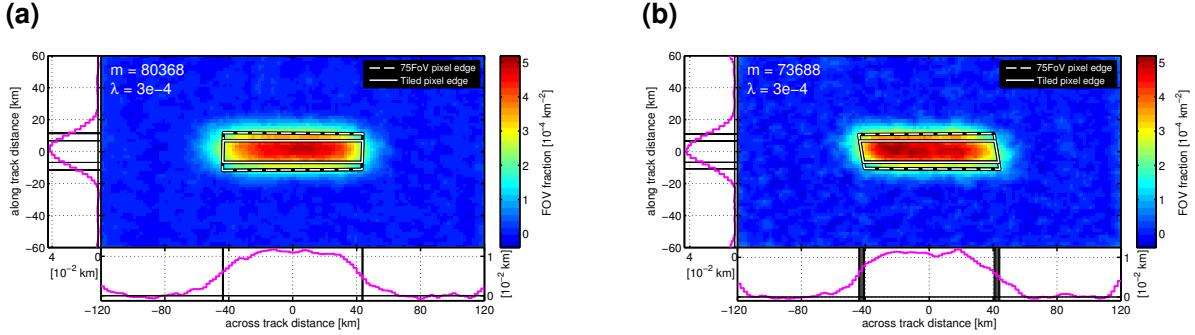
Figure 16. Same as in Fig. 13(c) but for OMI pixel 3 (western MODIS swath edge) and pixel 56 (eastern swath edge). Note that the retrieval ranges are adjusted to the increased nominal FOV size.

The FOV parametrisation Eq. (8) was fitted to the FOV results from pixel 3 through 56 (cf. Sect. 3.2.1 and Supplement). Figure 17 compiles the results for all three parameter classes: shape, width, and spatial offset with respect to the provided pixel centre in both directions, respectively. The shape parameters a_1 scatters around a minimum 3.5 in the swath centre and increases slowly to 4 and 4.5 at the western and eastern swath edge, respectively. In along-track direction, b_1 averages to 2.2 with comparatively small scatter and negligible viewing angle dependence.

The FOV widths show little scatter and depend on the viewing angle as expected (Fig. 17(b)). There are, however, differences when compared to the pixel widths provided in OMPIXCOR. In across-track direction, differences between retrieved FWHM width w_x and provided tiled pixel edges are negligible. In along-track direction, however, there are systematic differences. The

retrieved 75 % width is ≈ 1 km larger than 75FoV from OMPIXCOR at small viewing angles, whereas pixels at the swath edge (3–10 and 50–56) appear even narrower than provided.

Figure 17(c) reveals that the OMI pixel FOVs were systematically shifted in both dimensions. The displacement in across-track direction a_3 is negative outside the range between 10 and 30 km, i. e. the actual centre of the FOV was shifted westward (cf. Fig. 16(b)). The absolute across-track offset was maximal (> 1 km) at the swath edges. The viewing angle dependence of the spatial offset in along-track direction b_3 was clearly more complex, but still systematic and smooth. For the entire swath, b_3 is in the range between 1 and 1.5 km. At the swath edges, b_3 was always positive, i. e. a displacement towards north, which is ~~clearly~~ visible in Fig. 16.

3.3 SO$_2$-camera

The applicability of IFR to ground-based measurements is demonstrated using SO$_2$ apparent absorbance and SO$_2$ SCDs measured by an SO$_2$-camera and a LR-DOAS instrument, respectively. The iterative LSMR method was applied ($\lambda = 2.5 \times 10^{-4}$) because the number of correlated HR/LR measurements was limited. Furthermore, the same data was evaluated applying the correlation method for comparison (Sect. 2.1.3). Figure 18 shows the results of both methods. The exemplary SO$_2$ apparent absorbance image in Fig. 18(a) exhibits a linear distortion along the edge of the mountain (row number 240 and below). This distortion was caused by slight changes of the light path when different filters were applied.

For IFR, the size of the FOV was determined by fitting a Gaussian to the horizontal and vertical cross-section through the peak of the FOV result, respectively. The fit results then yielded a horizontal FWHM of 0.49 ° and a vertical FWHM of 0.42 °. For comparison, the correlation method obtained an almost perfect HR/LR correlation for a circular FOV with an angle of view diameter in the range between 0.4 ° and 0.9 ° with a maximum at 0.6 °. The maximum found by IFR seems to be significantly biased towards top-right. Numerically, however, the bias was small (0.35 and 1.2 pixel in horizontal and vertical direction, respectively) if the fit results of the two Gaussians above were applied. This behaviour may be due to the minor contributions in the retrieved FOV distribution to the lower left of the black circle.

4 Discussion

4.1 GOME-2

The FOV results for GOME-2 confirm that most of the actual measurement sensitivity is confined to the pixel edges provided by EUMETSAT – as long as spatial aliasing is corrected for. The spatial aliasing correction depends on the wavelength range of interest and, hence, on the retrieval of various properties, e. g. trace gas column, aerosol index, or cloud fraction. It is noted that the spatial aliasing effect for most retrievals is smaller than illustrated in Fig. 7(a) because the Gaussian 630 km convolution kernel applied covers the left edge of MSC channel 4, which is read-out last.

For the AVHRR/GOME-2 combination, HR and LR measurements are highly correlated because both instruments are mounted on the same spacecraft and, therefore, the temporal offset in the data is minimal. Different spectral convolution ker-
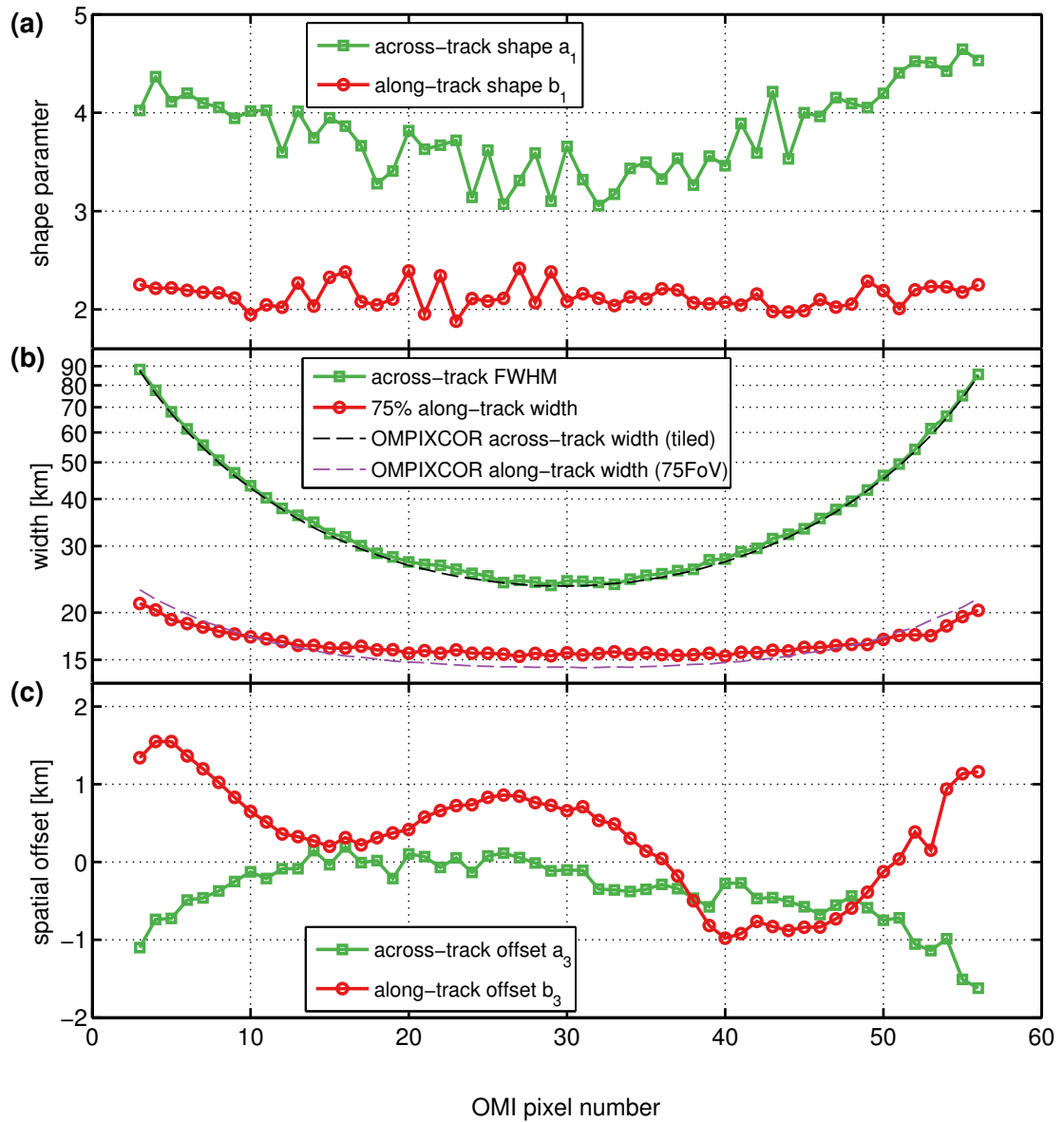
Figure 17. Dependence of the retrieved FOV parametrisation on OMI pixel number in across-track (green squares) and along-track (red circles) direction, respectively ($\lambda = 3 \times 10^{-4}$, $t_\mathrm{w} = 15$ m/s): (a) Shape parameters a_1 and b_1, (b) retrieved FOV widths compared to corresponding tiled and 75FoV pixel widths provided by OMPIXCOR, and (c) spatial offsets a_3 and b_3.
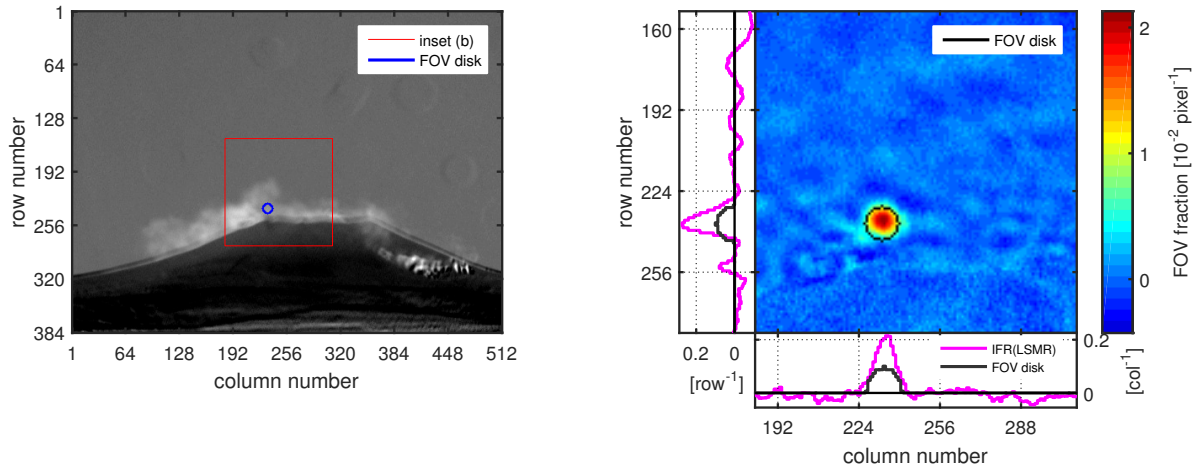
Figure 18. SO$_2$-camera data recorded on 21 November, 2014 at Lastarria volcano: (a) example apparent absorbance τ measured at 13:39:30 UTC (white areas correspond to large SO$_2$ column densities) illustrating the HR FOV, (b) comparison of retrieved FOV using the correlation method (0.6 $^\circ$ diameter FOV disk, circle is outer range) and IFR applying the LSMR method ($\lambda = 2.5 \times 10^{-4}$. The resolution of the SO$_2$-camera image is 512 pixel per 23.5 $^\circ$ corresponding to 0.046 $^\circ$/pixel.

nels for the LR measurements were tested in the course of this study and, surprisingly, the highest SNR has not been achieved using the spectral response of AVHRR channel 1 (cf. Figs. 2 and A1). Instead, the highest SNR has been achieved using a Gaussian-shaped convolution kernel centred at 630 nm with a FWHM similar to the spectral response of AVHRR channel 1.

The influence of spatial aliasing was minimised by using a spectral convolution kernel at the right edge of GOME-2 channel 5 4 where the detector readout starts. Therefore, a synthetic spectral response peaking at 780 nm was used to convolve LR measurements. The retrieval noise was found larger than with the above settings, even though measurements over land were filtered in order to reduce interferences with chlorophyll absorption. Section A) in the Appendix compiles a matrix analysis between different LR convolution kernels and HR channels and discusses the FOV retrieval error.

Furthermore, the FOV at the swath edge and for special scanning modes has been investigated. At the edge of the standard 10 1920 km swath, the FOV distributions of the MSC pixels are less homogeneous than in nadir direction. In particular, the moving direction of the scan-mirror changes during the integration of pixels 23 and 31 creating complex FOV distributions. Depending on the spatial aliasing, pixel 31 (last back-scan pixel) provides the best spatial resolution of all GOME-2 MSC pixels, which is, however, seldom used because most retrievals remove back-scan pixels from further processing by default.

It is observed that the FOV contributions decrease towards the swath edges in pixels 23 and 31. Furthermore, also the FOV 15 for pixel 0 (in Fig. 8(b)a) shows a significant gradient in scan-direction. It seems that the scan-mirror does not reach the intended turning point, maybe due to accumulated lubricant in the bearing of the stepper-motor. Then, the uneven FOV pattern of pixel 0 could be explained by a jitter of the actual mirror-position compared to the intended mirror-position. It is a known issue of the instrument design of GOME-2, that lubricant may accumulate at both turning points of the scanner after a certain

period of operation. Therefore, a continuous 360° mirror spinning during the night-side of the orbit has been introduced by GOME-2 operations in 2008 in order to mitigate the lubricant build-up. The spinning improved the mirror positioning statistics of GOME-2 as a whole (see daily reports on (EUMETSAT, 2015a)), but at the swath edges in particular, the mirror spinning is mitigating the issue not completely.

5   The residual χ^2 is not equal for all pixels. Especially pixels 5,6, and 29 suffer from an inferior SNR compared to the other pixels (Fig. 10). Furthermore, χ^2 increased towards the swath edges. The reasons for the inferior SNR can be manifold: (a) One explanation could be, that the mirror does not travel very smoothly in this viewing angle range leading to significant pointing error (jitter) which, in turn, would reduce the correlation for IFR. However, the position difference and current drawn by the stepper motor do not indicate a systematic problem between -30 and -25 ° scanner-angle (EUMETSAT, 2015a). (b) Another

10 hypothesis for the observed distortions, sun-glint, could be ruled out during preliminary tests where observations over ocean were excluded. (c) There may still be another reason for the increased noise at the swath edges. The resolution of the stepper motor at the swath edges is inferior to that at nadir because the motor speed is variable to maintain a regular pixel size in across-track direction (Munro et al., 2016). A pixel at the swath edge features less stepper motor steps and, hence, pointing accuracy decreases and positioning jitter increases as observed. (d) Erroneous AVHRR HR-imager data are another possibility.

15 A viewing angle dependent radiometric or pointing instability would propagate into the FOV results. For example, preliminary evaluations of the AVHRR data revealed systematic column-by-column variations which may interfere with IFR. The angular velocity of LR- and HR-instruments are different, which may increase viewing angle dependent interferences even further.

    As last examples for GOME-2 pixel shapes, the FOV of MSC narrow-mode and PMD pixels were investigated (Fig. 12). Periodic structures, as in Fig. 16 for OMI, are neither evident in along- nor across-track direction, even though always nine

20 neighbouring pixels within one scan were used. The FOV width in across-track direction of the PMD and narrow-mode nadir pixels are similar. This observation is surprising because the across-track PMD pixel edges were assumed much steeper. Furthermore, the observed across-track FOV shape is ascribed to the readout of the PMD channel 12. The total PMD readout lasts longer than the readout of a single PMD detector channel ($45.776\,\mu s$) due to the binning within each PMD channel as defined in Lang (2010). Another parameter leading to smoother edges in across-track direction may be the convolution with an IFOV

25 width of 4 km, which is much less prominent at regular swath widths.

    For the PMD channel, the spatial aliasing effect is less prominent compared to the MSC examples due to the different readout timing. It is furthermore observed that the across-track PMD FOV distribution is significantly narrower than suggested by the pixel edges and that it is shifted in scanning direction (to the left). However, satellite retrievals relying on an accurate mapping of AVHRR cloud-fractions data on GOME-2 PMD pixels like the Polar Multi-sensor Aerosol Product (PMAp EUMETSAT,

30 2015b) are potentially affected by the FOV differences found.

    The FOV integrated in along-track direction differs between PMD and narrow-mode pixels. While the narrow-mode FOV is as flat-topped as for regular MSC pixels (cf. Fig. 7a), the PMD FOV features a statistically significant variation of approximately 5%. This variation may be attributed to the different optical paths in the GOME-2 instrument possibly leading to different effective sensitivities across the aperture of the instrument.

It is finally noted for the $10 \times 40\,\mathrm{km}^2$ FOVs, that the pointing instabilities discussed above may have a minor impact on the MSC narrow mode alignment because the mirror moves slower. For the PMDs, however, the resulting distortions can be assumed more significant due to the 8 times higher resolution in across-track direction.

4.2 OMI

5 The retrieval of FOV for the OMI instrument is more complicated than for GOME-2. The application of a wind-speed filter increases the correlation between HR and LR measurements significantly. Despite the filter, however, the exact results still have higher noise levels, probably due to the orbital delay between the Aqua and Aura satellites. Therefore, an approximating numerical solver is applied, which also acts as a spatial low-pass filter.

The retrieved FOV shape and size are very close to the parameters prescribed in the technical documentation. Kurosu and 10 Celarier (2010) assume a fourth-order Gaussian as an along-track IFOV for OMI, which is then convolved with the platform movement during integration. This convolution was approximated by directly fitting a 2D super-Gaussian, which was found to describe the retrieved OMI FOV features very well. The differences between convolved and approximated version are minor (cf. Fig. 13(d)), and the fitted super-Gaussian seems to even better represent the retrieved FOV values than the theoretical FOV shape. ~~Therefore, the~~ In principle, the OMPIXCOR pixel edges suggest a skewed 2D super-Gaussian. However, the IFR 15 results obtained for OMI are not significantly skewed. The proposed 2D super-Gaussian therefore appears to be a sufficient approximation in this study, which could be implemented into standard gridding routines for OMI.

At the swath edge, the two provided pixel edges (tiled and 75FoV) deviate significantly and the 75FoV pixel edge apparently captures the retrieved FOV much better than the tiled pixel edge product. In the swath centre, the retrieved 75 % along-track widths are larger than the provided 75FoV widths, whereas the opposite is the case at the swath edges. It must be noted that the 20 presented results probably overestimate small FOV widths due to the effective smoothing of the LSMR solver in combination with residual cloud movement. It is therefore surprising that the provided 75FoV width actually seems to overestimate the true along-track width at the swath edges. This overestimation, however, only plays a minor role in the application of OMI data because many studies discard measurements with pixel numbers smaller than 10 and above 50 due to their inferior spatial resolution. It is furthermore noted that the provided FWHM widths in across-track direction are perfectly reproduced by this 25 study.

Furthermore, there is a systematic spatial offset of the FOV centre depending on the viewing angle. The offset is of the order of $\pm1\,\mathrm{km}$ in both directions, which is still within the instrument specification. The observed offset is apparently due to wavelength dependent properties of the OMI optics in general and the diamond effect of the polarisation scrambler in particular. It is noted that the temporal stability of the OMI geolocation offset is of the same order as investigated by Kroon et al. (2008) 30 during the years 2005–2006.

Towards the swath edges, ~~one type of IFR artefact appears~~a typical behaviour of IFR applying LSMR may be observed: The FOV increases towards the domain edges producing small wings of the along-track integrals (plotted in magenta at the bottom of both Figs. 16(a) and (b)). One possible explanation for this ~~artefact~~ behaviour may be atmospheric or instrumental straylight at these viewing angles. Numerical simulations ~~of the method~~ showed that additional random contributions, which

are not captured by the applied linear FOV model, can lead to this type of ~~artefact~~behaviour. Consequently, strong interferences for pixels affected by the row anomaly, which appeared later during the mission, were observed in preceding IFR experiments conducted at various grid sizes and resolutions. These results were not included into this paper due to the ambiguity of the interpretation. However, the FOV results of pixels 37–42 and 53–54 (see Supplement) are not significantly affected by the row

5   anomaly even though the measurements are actually affected according to KNMI (2015). Apparently, the influence of the row anomaly on IFR based on data recorded in October 2008 is negligible. In order to investigate the effect of row anomalies in the future, second order effects may be added to the linear IFR model presented in this paper.

It is finally noted that the results obtained for OMI in this study are in accordance to the FOV parameters derived by de Graaf et al. (2016), who presented a similar 2D parametrisation of the OMI FOV derived from correlated MODIS measurements.

10   The main difference between this work and de Graaf et al. (2016) is that we retrieved a discretised FOV prior fitting a 2D distribution, which required orders of magnitude more HR measurements. Hence, FOV structures different to an a-priori FOV parametrisation could, in principle, be retrieved. Furthermore, the FOV parametrisation applied by de Graaf et al. (2016) did not include any spatial shifts and parameters were obtained by looking for maximum correlation while changing the coefficients rather than by applying a least-squares fit. For OMI, however, the agreement between both approaches confirms the validity of

15   using a FOV model with only few parameters, which may not have been the case a-priori.

4.3 SO_2-camera

The FWHM values from the IFR results (0.49° and 0.42°) are at the lower end of the range obtained by the correlation method (0.4° to 0.9°) and compare very well to the theoretical FOV of 0.46°. Concerning the FOV shape, the results in Fig. 18b indicate some distortion from the flat disk approximation assumed for the correlation method. The IFR result reveals

20   an almost circular peak blurred to the lower left. The apparent FOV contribution at the bottom-left of the circle may be caused by a combination of temporal delay between HR and LR measurements as well as acquisition delay between I_A and I_B since the plume was moving into that direction. Furthermore, distortions at the mountain edge below row number 240 could have an influence. It is therefore difficult to judge whether this contribution to the FOV is real or not. Furthermore, the spatial smoothing caused by the LSMR method adds another uncertainty because $m = 2334$ was much smaller for the SO_2-camera compared

25   to satellite measurements and, therefore, it was not possible to retrieve the FOV at such a high spatial resolution. The size and shape of the artefacts are similar to the background noise structures whose average size results from the low-pass filtering effect.

The FOV results obtained in this study still add information about the actual FOV: the retrieved complexity, whether true or not, indicate that there is spatial heterogeneity in the correlation between LR and HR measurements, which cannot be resolved

30   by the correlation technique. This heterogeneity is probably the reason for the observed (tiny) differences in the results of the two compared techniques: (1) the bias between the IFR peak and the FOV disk in Fig. 18b, and (b) the FOV diameter could not unambiguously be retrieved by the correlation technique. Hence, we conclude that the actual FOV had probably the size of the theoretically computed diameter featuring steeper edges, which could not be resolved due to the limited sample size, and

that the correlation technique was overestimating the FOV diameter due to the spatial heterogeneities. In summary, however, the influence of the discussed differences on the measured SO_2 fluxes are probably minor.

It is noted that IFR is significantly faster than the state-of-the-art correlation technique, which, however, has not been tuned for speed. Using the same data basis, IFR using LSMR finished after 3.5 s while the brute-force implementation correlation technique by Lübcke et al. (2013) took as much as 1400 s to find the best LR/HR-correlation within the HR-FOV using just one a-priori FOV shape. Hence, a speed-up by a factor of 400 could be achieved although less a-priori information is required.

5 Conclusions

This paper describes IFR, which is an independent method ~~IFR~~ to characterise the effective FOV of instruments with low spatial resolution applying complimentary measurements at higher resolution during operation without the need of a dedicated, controlled lab environment. IFR was applied to three instruments: GOME-2 and OMI, which are both satellite instruments, and a ground-based MAX-DOAS instrument. The quality of existing FOV parametrisations was assessed using the independently retrieved FOV results.

For GOME-2, spatial aliasing is a known issue that has been ignored in most past studies. The effect is demonstrated using measurement data itself and the formulas correcting for this effect could be verified. Furthermore, specific artefacts caused by unexpected scanner operation could be identified. Future studies of the GOME-2 FOV may be conducted using the nadir-static mode of GOME-2 in which the scanner motor is locked. It should then be possible to retrieve the true IFOV of GOME-2 because the FOV movement during integration becomes negligible.

For OMI, only approximate solutions could be obtained due to to limited correlation caused by the orbital delay of 8 minutes between HR and LR measurement. The retrieved FOV distribution is much more complex than for GOME-2. While the FOV of GOME-2 is essentially rectangular, the OMI FOV could be parametrised using a 2D super-Gaussian FOV model. This FOV model is proposed for future operational use for imaging spectrometers because it is comparatively simple, yet providing sufficient accuracy.

The complexity of the retrieved FOV is expected to inspire more sophisticated treatment of the geolocation of each individual pixel. We see five major applications of more accurate satellite FOV models: (1) Correlations between ground-based and satellite measurements, (2) high-resolution mapping of atmospheric pollutants, e. g. NO_2 from TROPOMI/S-5P, (3) mapping of HR cloud products on the respective LR measurements, (4) retrievals and studies using satellite data incorporating external data sources like albedo and sea-ice maps, and (5) comparisons between satellite measurements and independent data sets like model results. In any case, an insufficient knowledge of the FOV or ignoring the spatial aliasing in particular, introduce avoidable errors. It is noted that some of these issues have already been addressed, e. g. the pre-launch instrument calibration of TROPOMI displays a breakthrough for treating the FOV of spectrometers (Leloux, 2016) emphasising the importance of the topic.

For the SO_2-camera, IFR produced comparable results as the frequently used correlation method, but it is at least three orders of magnitude faster. IFR is furthermore independent from a-priori assumptions about the FOV shape, which renders the

method ideal for monitoring the DOAS-FOV shape and position in the field. However, interferences with plume movement and acquisition time differences may introduce artefacts in the result.

IFR is particularly efficient and easy to implement. Reasonable results were obtained also for underdetermined problems, for which, however, an error estimation is more difficult (Yao et al., 1999). The authors hope that this study will inspire SO_2-camera-operators and instrument developers to use the proposed method in order to monitor their FOV pointing and shape on a regular basis. The same applies to satellite instruments, whose FOV parameters may actually change during operation and which are usually inaccessible for calibration experiments after launch. In another recently published study, Verhoelst et al. (2015), the actual mapping of satellite sensitivity is discussed in great detail. Studies like this, where the focus lays in the comparison to ground-based measurements, significantly depend on the FOV of the satellite, whose actual distribution can now be assessed and monitored during operation more efficiently.

Vice versa, also radiometric calibration of satellite borne instruments (e. g. McCorkel et al., 2015) will probably benefit from better knowledge of the FOV. In particular, it should be possible to retrieve the spectral response functions of HR instruments from co-located LR measurements (Richard Siddans, pers. comm.).

Appendix A: Error estimation

The measurement errors of the input data applied in this study are not known a-priori. ~~It~~ In case of the standard least-squares solution, it is, however, still possible to estimate the goodness of the ~~standard least-squares solution~~ fit result c from the reduced χ^2, which is defined as the weighted sum of squared errors divided by the degrees of freedom. Assuming uncorrelated measurement errors and without weighting,

$$\chi^2 = \frac{F}{m - n'} \tag{A1}$$

where

$$F = \sum\nolimits_{p=1}^{m} r_{pk}^{2} \tag{A2}$$

is the variance of the residual $r = l - \mathbf{H}c$, and $m\text{-}n' = m\text{-}(n+1)$ approximates the number of degrees of freedom. The diagonal elements of the variance-covariance matrix

$$\Sigma = \chi^2 (\mathbf{H}^T \mathbf{H})^{-1} \tag{A3}$$

are now equal to the squared measurement standard deviations

$$\sigma_{kj} = \sqrt{(\Sigma_c)_{k,k}} \sqrt{(\Sigma_c)_{j,j}} \tag{A4}$$

for $kj = 0 \ldots n$.

However, degradation of both HR and LR instruments may further reduce the correlation within the data and, hence, possibly increase the actual error of c_j. Therefore, the estimated mean standard deviation $\bar{\sigma} = \overline{\sigma_j}$ is compared to the *empirical*

standard deviation $\hat{\sigma}$ in order to test the validity of the assumptions. $\hat{\sigma}$ is the standard deviation of a manually defined subset of the retrieved ~~e_k for which e_k~~ c_j for which c_j = 0 is assumed, i. e. grid points outside the inferred FOV.

For IFR applying the LSMR method, however, the ability to obtain error estimates are limited as pointed out by Yao et al. (1999), because the generalised inverse is not solved explicitly and neither the covariance nor the resolution matrix are provided.

5 Therefore, the error is not estimated in cases where LSMR was applied, i. e. for OMI and the ground-based DOAS.

A1 Example: GOME-2

Before comparing estimated mean standard deviation $\bar{\sigma}$ and empirical standard deviation $\hat{\sigma}$, a matrix analysis of $\hat{\sigma}$ was performed for GOME-2 pixel 12. $\hat{\sigma}$ was calculated for all LR/HR combinations using all five LR spectral convolution kernels and both short-wave AVHRR channels (Sect. 2.1.1 and Fig. 2). Furthermore, the analysis was conducted both on all $m = 100,000$

10 measurements and after measurements over land were removed in order to avoid interferences with chlorophyll absorption and resulting in $m = 61,066$. $\hat{\sigma}$ was calculated from the FOV results outside a rectangular mask potentially containing FOV contributions: values inside -60 km $< x <$ 44 km and -24 km $< y <$ 24 km were discarded.

The results in Fig. A1 show that the lowest empirical standard deviation $\hat{\sigma}$ was achieved using unfiltered LR and HR data applying the 630 nm LR convolution kernel and AVHRR channel 1, respectively. Apparently, the higher number of measurements

15 outweighs the correlation increase by the ocean filter. However, for GOME-2 measurements at longer wavelengths > 700 nm, where spatial aliasing is reduced, including only measurements over ocean significantly increases the quality of the results only if AVHRR channel 1 is applied but not for AVHRR channel 2. It is noted that applying the filter improved $\hat{\sigma}$ for LR/HR comparisons across the red-edge in general as expected: $\hat{\sigma}$ was significantly decreased for short-wave LR versus long-wave HR and vice-versa (yellow and orange colours in Fig. A1(b) compared to red colours ($\hat{\sigma} > 5 \times 10^3$) in Fig. A1(a)).

20 After the optimal LR/HR combination for GOME-2 was found, the dependence of $\bar{\sigma}$ and $\hat{\sigma}$ on sample number m and ocean ~~filer~~ filter was investigated. ~~This study was performed using AVHRR channel 1 and the 630nm LR convolution kernel.~~ Figure A2 illustrates the results using random selections of the basic populations of all data and data collected over ocean only. For sufficiently large $m \approx 5 \times 10^3$, it was observed that (1) the slopes were proportional to $m^{-1/2}$ (dashed purple lines), (2) excluding pixels over land improved retrieval noise, and (3) the empirical standard deviations were larger than those inferred

25 from theoretical considerations.

These results lead to the conclusion that the inter-pixel variations in the discrete FOV grid are, in principle, independent and that the theoretical limit has not been reached for $m = 10^5$. Hence, the noise of IFR results may be further reduced by increasing m. There are, however, signs that there are systematic biases, whose importance may increase at larger m. For constant m, the retrieval standard deviation decreases if pixels over land are filtered. This indicates that there are differences in the spectral

30 response between HR and LR measurement. The observation that $\bar{\sigma}$ underestimates $\hat{\sigma}$ has at least two possible explanations: (1) $\bar{\sigma}$ does not include all error contributions and (2) there are FOV contributions from outside the FOV mask used for calculating $\hat{\sigma}$. It may be however followed that $\hat{\sigma}$ is an appropriate error estimator.
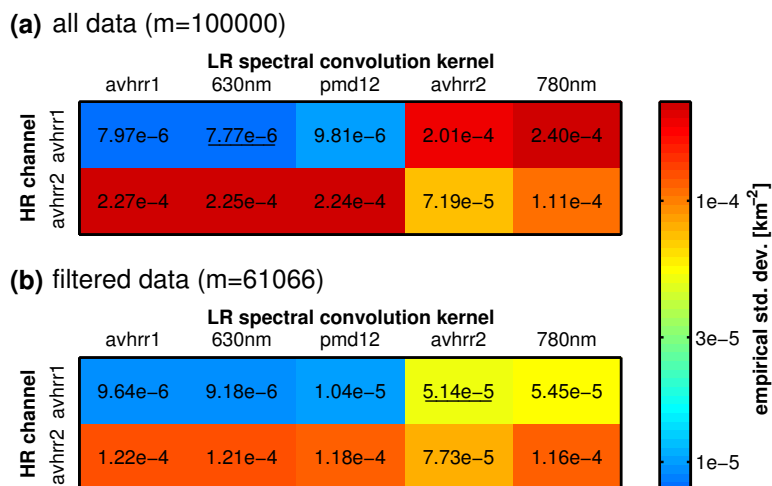
Figure A1. Empirical standard deviation $\hat{\sigma}$ depending on LR spectral convolution kernel, HR channel. The matrix analysis is performed (a) on unfiltered data and (b) on a subset containing only measurements over ocean to avoid interference with chlorophyll absorption. The underlined parameter combinations feature lowest $\hat{\sigma}$ values for the lower ($<700\,\text{nm}$) and the upper ($>700\,\text{nm}$) wavelength range in Fig. 2, respectively.

Acknowledgements. Holger Sihler acknowledges funding from the DLR Bonn under contract 50EE124 within the TROPOMI verification. Richard Siddans (RAL), Katja Grossmann (IUP), and Bert van den Oord (KNMI) are acknowledged for inspiring discussion and for technical assistance, respectively. Many people were involved in building the SO_2-camera prototype, P. Lübcke acknowledges in particular the work of Sebastian Illing and Marco Huwe (both IUP) and helpful tips for the design by Denis Pöhler. The SO_2-camera measurements were performed in the scope of the IAVCEI 12th Workshop on Volcanic gases. Help during measurements by Nicole Bobrowski, Florian Dinger and Ulrich Platt (all IUP) was gratefully received. GOME-2 and AVHRR level-1 data have been provided by EUMETSAT. OMI level-1 data have been provided by NASA and downloaded from the Goddard Earth Sciences Data and Information Services Center (GES DISC). MODIS level-1 data have been provided by NASA and downloaded from Level 1 and Atmosphere Archive and Distribution System (LAADS). ECMWF operational data have been obtained from the ECMWF Data Server.
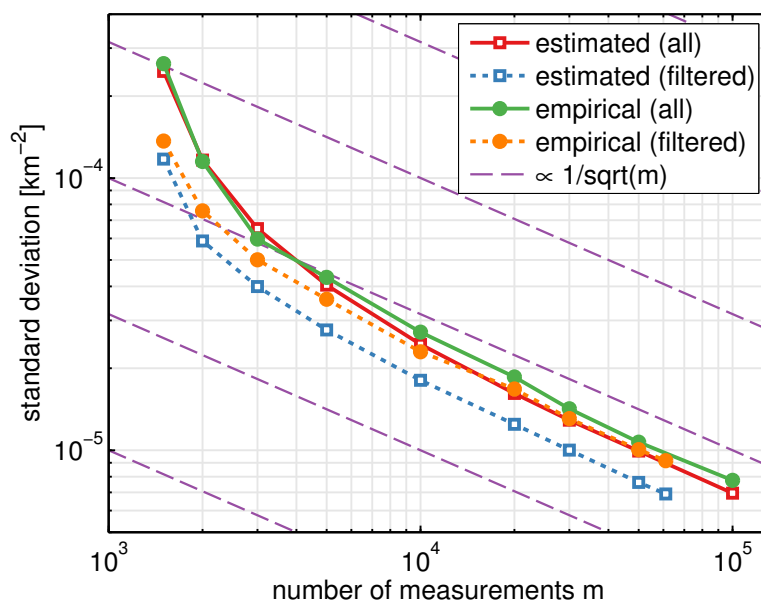
Figure A2. Comparison of estimated mean standard deviation $\bar{\sigma}$ (empty squares) and empirical standard deviation $\hat{\sigma}$ (filled circles) depending on number of measurements m included. The results denoted 'filtered' (dotted lines) are solely based on measurements over ocean. LR convolution kernel is centred at 630 nm and HR data is from AVHRR channel 1.

References

Barnes, W., Pagano, T. S., and Salomonson, V.: Prelaunch Characteristics of the Moderate Resolution Imaging Spectroradiometer (MODIS) on EOS-AM1, IEEE Trans. Geosci. Remote Sens., 36, 1088–1100, doi:10.1109/36.700993, 1998.

Bluth, G. J. S., Shannon, J. M., Watson, I. M., Prata, A. J., and Realmuto, V. J.: Development of an ultra-violet digital camera for volcanic
5   SO$_2$ imaging, J. Volcanol. Geoth. Res., 161, 47–56, doi:10.1016/j.jvolgeores.2006.11.004, 2007.

Callies, J., Corpaccioli, E., Eisinger, M., Hahne, A., and Lefebvre, A.: GOME-2 – MetOp's Second-Generation Sensor for Operational Ozone Monitoring, ESA Bulletin, 102, 28–36, 2000.

Campagnolo, M. L. and Montaño, E. L.: Estimation of Effective Resolution for Daily MODIS Gridded Surface Reflectance Products, IEEE Trans. Geosci. Remote Sens., 52, 5622–5632, doi:10.1109/TGRS.2013.2291496, 2014.

10 Cracknell, A.: The Advanced Very High Resolution Radiometer, Taylor and Francis, London, ISBN 9780748402090, 1997.

de Graaf, M., Sihler, H., Tilstra, L. G., and Stammes, P.: How big is an OMI pixel?, Atmos. Meas. Tech., 9, 3607–3618, doi:10.5194/amt-9-3607-2016, 2016.

Dobber, M. R., Dirksen, R. J., Levelt, P. F., van den Oord, G. H. J., Voors, R., Kleipool, Q., Jaross, G., Kowalewski, M., Hilsenrath, E., Leppelmeier, G., de Vries, J., Dierssen, W., and Rozemeijer, N.: Ozone Monitoring Instrument calibration, IEEE Trans. Geosci. Remote
15 Sens., 44, 1209–1238, doi:10.1109/TGRS.2006.869987, 2006.

EUMETSAT: AVHRR Level 1b Product Guide, Internet, http://www.eumetsat.int/website/wcm/idc/idcplg?IdcService=GET_FILE& dDocName=PDF_AVHRR_L1B_PRODUCT_GUIDE&RevisionSelectionMethod=LatestReleased&Rendition=Web, last access: 20 Oktober 2016, 2011a.

EUMETSAT: GOME-2 FM2-2 Calibration: field of view, ftp://ftp.eumetsat.int/pub/EPS/out/GOME/Calibration-Data-Sets/ Calibration-Key-Data/FM2-Metop-B/, doc. MO.TR-TPD-Gc-0122 in GOME-2 FM2 key data issue 2, 2011b.

EUMETSAT: EPS Product Quality Monitoring Reports – MetOp-A: GOME-2, Internet, http://oiswww.eumetsat.int/epsreports/html/index. php?instrument=GOME&sat=M02, last access: 20 November 2015, 2015a.

EUMETSAT: Polar Multi-Sensor Aerosol Product: ATBD, Tech. Rep. EUM/TSS/SPE/14/739904, EUMETSAT, http://www.eumetsat.int/ website/wcm/idc/idcplg?IdcService=GET_FILE&dDocName=PDF_PMAP_ATBD_PFS&RevisionSelectionMethod=LatestReleased, issue v3B, 2015b.

EUMETSAT: GOME-2 Factsheet, Internet, http://www.eumetsat.int/, Doc. No. EUM/OPS/DOC/10/1299, Issue v4B, 17 March 2015, 2015c.

Fong, D. C.-L. and Saunders, M. A.: LSMR: An iterative algorithm for sparse least-squares problems, SIAM J. Sci. Comput., 33, 2950–2971, published electronically Oct 27, 2011.

Kern, C., Kick, F., Lübcke, P., Vogel, L., Wöhrbach, M., and Platt, U.: Theoretical description of functionality, applications, and limitations of SO_2 cameras for the remote sensing of volcanic plumes, Atmos. Meas. Tech., 3, 733–749, doi:10.5194/amt-3-733-2010, 2010.

Kern, C., Lübcke, P., Bobrowski, N., Campion, R., Mori, T., Smekens, J.-F., Stebel, K., Tamburello, G., Burton, M., Platt, U., and Prata, F.: Intercomparison of SO_2 camera systems for imaging volcanic gas plumes, J, Volcanol. Geoth. Res., 300, 22–36, doi:10.1016/j.jvolgeores.2014.08.026, 2015a.

Kern, C., Sutton, J., Elias, T., Lee, L., Kamibayashi, K., Antolik, L., and Werner, C.: An automated SO_2 camera system for continuous, real-time monitoring of gas emissions from Kīlauea Volcano's summit Overlook Crater, J, Volcanol. Geoth. Res., 300, 81–94, doi:10.1016/j.jvolgeores.2014.12.004, 2015b.

KNMI: Background information about the Row Anomaly in OMI, Internet, http://www.knmi.nl/omi/research/product/ rowanomaly-background.php, last access: 24 February 2016, 2015.

Koelemeijer, R. B. A., Stammes, P., and Watts, P. D.: Comparison of Visible Calibrations of GOME and ATSR-2, Remote Sens. Environ., 63, 279–288, 1998.

Kroon, M., Dobber, M. R., Dirksen, R., Veefkind, J. P., van den Oord, G. H., and Levelt, P. F.: Ozone Monitoring Instrument geolocation verification, J. Geophys. Res., 113, D15S12, doi:10.1029/2007JD008821, 2008.

Kuhlmann, G., Hartl, A., Cheung, H. M., Lam, Y. F., and Wenig, M. O.: A novel gridding algorithm to create regional trace gas maps from satellite observations, Atmos. Meas. Tech., 7, 451–467, doi:10.5194/amt-7-451-2014, 2014.

Kurosu, T. P. and Celarier, E. A.: OMIPIXCOR Readme File, Internet, http://disc.sci.gsfc.nasa.gov/Aura/data-holdings/OMI/documents/ v003/OMIPIXCOR_README_V003.pdf, last access: August 2014, 2010.

Lang, R.: GOME-2 PMD Band Definitions 3.0 and PMD Calibration, EUMETSAT, http://www.eumetsat.int, Doc.No. EUM/OPS-EPS/DOC/07/0601, Issue v8, 2010.

Leloux, J.: readme for TROPOMI pixel response function, Memo, KNMI, http://www.tropomi.eu/sites/default/files/files/ S5P-KNMI-OCAL-0150-ME-readme_for_TROPOMI_pixel_response_function-1.0.0-20160401.pdf, issue 1.0.0, 2016.

Levelt, P. F., van den Oord, G. H. J., Dobber, M. R., Malkki, A., Visser, H., de Vries, J., Stammes, P., Lundell, J. O. V., and Saari, H.: The Ozone Monitoring Instrument, IEEE Trans. Geosci. Remote Sens., 44, 1093–1101, doi:10.1109/TGRS.2006.872333, 2006.

Lübcke, P., Bobrowski, N., Illing, S., Kern, C., Alvarez Nieves, J. M., Vogel, L., Zielcke, J., Delgado Granados, H., and Platt, U.: On the absolute calibration of SO_2 cameras, Atmos. Meas. Tech., 6, 677–696, doi:10.5194/amt-6-677-2013, 2013.

McCorkel, J., Cairns, B., and Wasilewski, A.: Imager-to-radiometer inflight cross calibration: RSP radiometric comparison with airborne and satellite sensors, Atmos. Meas. Tech. Discuss., 8, 10 361–10 386, doi:10.5194/amtd-8-10361-2015, 2015.

5 McGillem, C. D., Anuta, P. E., Malaret, E., and Yu, K. B.: Estimation of a remote sensing system point-spread function from measured imagery, LARS Technical Reports 81, Purdue University, http://docs.lib.purdue.edu/larstech/81, 1983.

Mori, T. and Burton, M.: The SO_2 camera: A simple, fast and cheap method for ground-based imaging of SO_2 in volcanic plumes, Geophys. Res. Lett., 33, L24 804, doi:10.1029/2006GL027916, 2006.

Munro, R., Eisinger, M., Anderson, C., Callies, J., Corpaccioli, E., Lang, R., Lefebvre, A., Livschitz, Y., and Albiñana, A. P.: GOME-2 on
10 MetOp, in: Proc. of The 2006 EUMETSAT Meteorological Satellite Conference, Helsinki, Finland, 12–16 June 2006, EUMETSAT, p. 48, 2006.

Munro, R., Lang, R., Klaes, D., Poli, G., Retscher, C., Lindstrot, R., Huckle, R., Lacan, A., Grzegorski, M., Holdak, A., Kokhanovsky, A., Livschitz, J., and Eisinger, M.: The GOME-2 instrument on the Metop series of satellites: instrument design, calibration, and level 1 data processing – an overview, Atmos. Meas. Tech., 9, 1279–1301, doi:10.5194/amt-9-1279-2016, 2016.

15 NASA: The Afternoon Constellation, http://atrain.nasa.gov/, last access: February 2015, 2014.

NOAA: NOAA-KLM User's Guide – Section 3.1, Website, http://www.ncdc.noaa.gov/oa/pod-guide/ncdc/docs/klm/html/c3/sec3-1.htm, last updated 3 March 2009, last access 20 Oktober 2016, 2009.

NOAA: NOAA KLM User's Guide – Appendix D.5, Website, http://www.ncdc.noaa.gov/oa/pod-guide/ncdc/docs/klm/html/d/app-d5.htm, last updated 13 April 2009, last access 20 Oktober 2016, 2014.

20 Paige, C. C. and Saunders, M. A.: LSQR: An Algorithm for Sparse Linear Equations And Sparse Least Squares, ACM Trans. Math. Soft., 8, 43–71, 1982.

Platt, U. and Stutz, J.: Differential Optical Absorption Spectroscopy – Principles and Applications, Springer, Berlin, Heidelberg, New York, 1st edn., 2008.

Ruiz, C. P. and Lopez, F. J. A.: Restoring SPOT images using PSF-derived deconvolution filters, Int. J. Remote Sensing, 23, 2379–2391,
25 doi:10.1080/01431160110075857, 2002.

Salomonson, V., Barnes, W., Maymon, P. W., Montgomery, H., and Ostrow, H.: MODIS: Advanced Facility Instrument for Studies of the Earth as a System, IEEE Trans. Geosci. Remote Sens., 27, 145–153, doi:10.1109/36.20292, 1989.

Schoeberl, M. R.: The afternoon constellation: a formation of Earth observing systems for the atmosphere and hydrosphere, in: International Geoscience and Remote Sensing Symposium (IGARRS), Toronto, Canada, 24–28 June 2002, vol. 1, pp. 354–356, IEEE,
30 doi:10.1109/IGARSS.2002.1025038, 2002.

Schoeberl, M. R., Douglass, A. R., Hilsenrath, E., Bhartia, P. K., Beer, R., Waters, J. W., Gunson, M. R., Froidevaux, L., Gille, J. C., Barnett, J. J., Levelt, P., and DeCola, P.: Overview of the EOS aura mission, IEEE Trans. Geo. Rem. Sens., 44, 1066–1074, doi:10.1109/TGRS.2005.861950, 2006.

Siddans, R.: S5P-NPP Cloud Processor, ATBD, RAL Space, http://www.tropomi.eu/sites/default/files/files/S5P-NPPC-RAL-ATBD-0001_
35 NPP-Clouds_v1p0p0_20160212.pdf, issue 1.0.0, 2016.

Smekens, J.-F., Clarke, A. B., Burton, M. R., Harijoko, A., and Wibowo, H. E.: SO_2 emissions at Semeru volcano, Indonesia: Characterization and quantification of persistent and periodic explosive activity, J. Volcanol. Geoth. Res., 300, 121–128, doi:10.1016/j.jvolgeores.2015.01.006, 2015.

te Plate, M. B., Draaisma, F., de Vries, J., and van den Oord, G. H. J.: Ozone Monitoring Instrument: system description and test results, in: Proc. SPIE 4540 – Sensors, Systems, and Next-Generation Satellites V, edited by Fujisada, H., Lurie, J. B., and Weber, K., p. 122, doi:10.1117/12.450654, 2001.

Tilstra, L. G., Tuinder, O. N. E., and Stammes, P.: GOME-2 PMD band reflectances – verification report, KNMI Report KNMI-RP-2011-01, http://www.knmi.nl/~tilstra/Reports/KNMI-RP-2011-01.pdf, 2011.

Verhoelst, T., Granville, J., Hendrick, F., Kühler, U., Lerot, C., Pommereau, J.-P., Redondas, A., Van Roozendael, M., and Lambert, J.-C.: Metrology of ground-based satellite validation: co-location mismatch and smoothing issues of total ozone comparisons, Atmos. Meas. Tech., 8, 5039–5062, doi:10.5194/amt-8-5039-2015, 2015.

Wang, Z., Xiong, X., Choi, T., and Link, D.: On-Orbit Characterization of MODIS Modulation Transfer Function Using the Moon, IEEE Trans. Geo. Rem. Sens., 52, 4112–4121, doi:10.1109/TGRS.2013.2279610, 2014.

Wolfe, R. E., Lin, G., Nishihama, M., Tewari, K. P., Tilton, J. C., and Isaacman, A. R.: Suomi NPP VIIRS prelaunch and on-orbit geometric calibration and characterization, J. Geophys. Res. Atmos., 118, 11 508–11 521, doi:10.1002/jgrd.50873, 2013.

Xiong, X., Che, N., and Barnes, W.: Terra MODIS On-Orbit Spatial Characterization and Performance, IEEE Trans. Geosci. Remote Sens., 43, 355–365, doi:10.1109/TGRS.2004.840643, 2005.

Xiong, X., Che, N., and Barnes, W.: Terra MODIS On-Orbit Spectral Characterization and Performance, IEEE Trans. Geosci. Remote Sens., 44, 2198–2206, doi:10.1109/TGRS.2006.872083, 2006.

Xiong, X., Sun, J., Che, N., Angal, A., and Choi, J.: Comparison of Terra and Aqua MODIS VIS Bands On-Orbit Response, in: International Geoscience and Remote Sensing Symposium (IGARSS), Boston, USA, 7–11 July 2008, vol. 4, pp. 1348–1351, IEEE, doi:10.1109/IGARSS.2008.4779981, 2008.

Yao, Z. S., Roberts, R. G., and Tryggvason, A.: Calculating resolution and covariance matrices for seismic tomography with the LSQR method, Geophys. J. Int., 138, 886–894, 1999.